This document was prepared for the ETI by third parties under contract to the ETI. The ETI is making these documents and data available to the public to inform the debate on low carbon energy innovation and deployment.

Programme Area: Marine

Project: PerAWAT

Title: Non-Linear Model Description Report

Abstract:

This report introduces the methodology to be used for assessing the fully nonlinear hydrodynamic response of wave energy converters (single devices and arrays of point absorbers). It describes the key steps for implementing the boundary element potential flow model OXPOT, addressing issues such as the formulation of higher order elements and discontinuous elements, mesh generation and regridding, use of an artificial damping layer, time stepping, and the use of domain decomposition to improve computational efficiency. Examples of implementation of the model are given, including comparison of results with experimental data. Additionally, by way of introduction, the report briefly raises some technical issues which might be addressed in the development of a design methodology for wave energy converters. Several of these were investigated in the course of obtaining results reported in subsequent deliverables. Furthermore, the report also outlines the intended stages of applying the nonlinear methodology, including the evaluation of a range of cases of increasing realism and complexity. Consideration is also given to modelling the behaviour of wave energy converters in both regular and irregular seas.

Context:

The Performance Assessment of Wave and Tidal Array Systems (PerAWaT) project, launched in October 2009 with £8m of ETI investment. The project delivered validated, commercial software tools capable of significantly reducing the levels of uncertainty associated with predicting the energy yield of major wave and tidal stream energy arrays. It also produced information that will help reduce commercial risk of future large scale wave and tidal array developments.

Energy Technologies Institute

PerAWaT

WG1 WP1 D7: Non-Linear Model Description Report

Authors P. H. Taylor and R. Eatock Taylor

Version 1.0

Date 23rd April 2010

Revision History		
Issue / Version	Issue Date	Summary
0.1	27/04/10	Submitted to GH
1.0	28/04/10	Updated following comments by GH

Context

This report is the first deliverable Numbered D7 from the UoO work on the wave energy stream of the PerAWaT project. It introduces the methodology to be used for assessing the fully nonlinear hydrodynamic response of wave energy converters (single devices and arrays of point absorbers). The report describes the key steps for implementing the boundary element potential flow model OXPOT, addressing issues such as the formulation of higher order elements and discontinuous elements, mesh generation and regridding, use of an artificial damping layer, time stepping, and the use of domain decomposition to improve computational efficiency. Examples of implementation of the model are given, including comparison of results with experimental data.

Additionally, by way of introduction, the report briefly raises some technical issues which might be addressed in the development of a design methodology for wave energy converters. Several of these will be investigated in the course of obtaining results to be reported in subsequent UoO deliverables. Furthermore, the report also outlines the intended stages of applying the nonlinear methodology, including the evaluation of a range of cases of increasing realism and complexity. Consideration is given to modelling the behaviour of wave energy converters in both regular and irregular seas.

Issues of validation are to be addressed through comparison with experimental results from WG2 WP1 and WG2 WP2. The results for the nonlinear model will then be used in an assessment of the accuracy of linear models applied to various scenarios.

Table of Contents

List of figures

1. Introduction

Study of the interaction of waves with arrays of structures, including wave energy devices, has been almost exclusively based on linear theory. This has led to considerable insight into the phenomenon of near-trapping (e.g. Linton and Evans 1990, Evans and Porter 1997, Maniar and Newman 1997, Walker and Eatock Taylor 2005). In this, very large localised wave elevations are predicted, due to quasi-resonant standing wave effects arising from the interference of waves radiated by adjacent structures. Most linear analyses of near-trapping have been concerned with multiple fixed structures. Work has also been done on moving structures such as semisubmersibles, tension leg platforms, and mobile offshore bases, where the multiple columns are closely spaced but the units comprising several columns move as rigid bodies. Rather little research has been conducted on the phenomenon of near-trapping in independently oscillating closely space structures. Siddorn and Eatock Taylor (2008) used linear analysis to investigate such effects in the case of four independently oscillating columns, and some implications for wave energy arrays were considered by Cruz et al (2009).

As near-trapping is quasi-resonant behaviour, one must consider the likelihood of significant response in transient wave packets. Still in the context of linear theory, some preliminary consideration has been given to this by Eatock Taylor (2007), Eatock Taylor and Meylan (2007) and Meylan and Eatock Taylor (2009).

Limited attempts have been made to investigate near-trapping using second order analysis. Malenica et al (1999) applied a frequency domain model to this problem, and demonstrated that large interactions due to second order diffraction can occur due to incident waves at half the frequency of waves exciting linear near-trapping. Walker et al (2008) studied this type of second order behaviour in the context of a realistic gravity based structure, and showed that even in transient wave groups the phenomenon can lead to very large localised wave elevations. Because of the effect of frequency doubling, significant second order near-trapping can be excited at wave frequencies which are too low to cause linear trapping responses. Wang and Wu (2007) have used a second order time domain finite element model to study near-trapping in arrays, which could potentially be used to investigate behaviour in transient wave packets – though the results in that

paper are concerned with the build–up of the phenomenon in regular waves.

Wang and Wu (2010) have gone on to develop a fully nonlinear finite element model. They have applied this to the diffraction of waves by closely spaced cylinders, and found some evidence of near-trapping. It appears, however, that up to now there has been no systematic study anywhere of the implications on nonlinearities in the near-trapping phenomenon. It is particularly important to understand this in the context of independently oscillating bodies comprising arrays of wave energy converters (WECs).

There are several technical issues that need to be resolved in development of a soundly based technology for designing arrays of WECs. These include matters related to the physical processes governing the performance of arrays, and issues related to the type of tools which may be used in the optimisation of designs of WEC arrays under both performance and survival conditions. Concerning the physical processes, some of the questions which might be asked include the following.

- What are the implications of near-trapping on average power take-off in regular waves?
- How significant are (linear) near-trapping effects in non-periodic waves; e.g. in transient wave packets?
- If near-trapping effects can be exploited to optimise average power under operational conditions, what might be the consequences for behaviour under extreme conditions?
- Could there be advantages in using non-regular spacing of elements in an array of WECs?
- What is the interaction between realisable power take-off (PTO) systems and the phenomenon of near-trapping?

In relation to the design methodology for optimising arrays of WECs, there are vital matters concerning validation of software tools and verification of the models underlying the design process. In order to span very large parameter spaces in design optimisation, it would seem desirable to be able to base models on the assumptions of linear theory and the representation of the hydrodynamics by potential flow theory. Some relevant questions are as follows.

- What are the effects of viscous damping, which is absent from potential flow models?

- For compact structures, important parameters governing the significance of nonlinearities are wave steepness and the ratio of wave height to a length parameter such as column diameter (Faltinsen et al 1995, Malenica and Molin 1995). What role does the spacing between bodies in an array play in triggering nonlinear effects linked to near trapping?
- How does the above depend on the differences between periodic and transient waves?
- How are the answers to the above questions dependent on the constraints imposed on the system by the PTO?

The approach being taken at Oxford University for the waves work in the PerAWaT programme has been designed to elucidate these issues. It is based on a nonlinear potential flow tool, OXPOT, which has been developed over recent years at Oxford, and implemented for some analyses of single bodies in waves and excited by prescribed forcing. The technical background to OXPOT, and some examples of its application, are given in the next section of this report. This is followed by a description of the methodology which is being adopted to apply OXPOT to the modelling of WEC arrays, with the objective of shedding light on the questions raised above. The approach involves three linked components:

- analyses of generic cases of increasing complexity, using OXPOT, to develop understanding of the effects of geometry, wave environment and PTO on WEC responses and available power;
- Comparison with results from experimental data made available through the PerAWaT programme, to validate the model;
- comparisons with results from the WaveFarmer software under development at Garrad Hassan, particularly to identify any important effects of non-linearities.

2. The nonlinear hydrodynamic model

2.1 Introduction to OXPOT

During the last two decades, the nonlinear time-domain simulation of bodies in steep waves, having applications to load, response and wave profile predictions for offshore structures, have attracted a great deal of attention. New methods have been developed and applied in parallel with the rapid growth of computer power. Such methods must deal with a major difficulty, namely that the complicated nonlinear free surface boundary conditions have to be satisfied on the instantaneous free surface not known a priori. Generally speaking, two approaches have been used to deal with this problem. One uses a perturbation expansion with respect to wave steepness, and the Taylor approximation of boundary conditions on the mean water and body surfaces. Molin (1979), Eatock Taylor and Hung (1987), Kim and Yue (1989), and Newman (1990), for example, used such a method at second-order for wave diffraction problems in the frequency domain. This approach is only suitable for weakly nonlinear waves, as it becomes much more complex at higher order. For regular waves, however, Malenica and Molin (1995) solved the diffraction problem at third order for a vertical cylinder, and a numerical solution for axisymmetric bodies was developed by Teng and Kato (2002). These perturbation expansion methods have also been applied in time-domain calculations, for example by Isaacson and Cheung (1992), Kim et al. (1997) and Wang and Wu (2007), to investigate second-order wave diffraction. An advantage of such an approach compared with fully nonlinear time domain simulations is that the coefficient matrix of the linear equation system is the same at each time step.

The other widely used approach is the fully nonlinear time-domain method, introduced for waves in the absence of diffracting bodies by Longuet-Higgins and Cokelet (1976). They used a Mixed Eulerian- Lagrangian (MEL) time stepping technique. By this method, the fully nonlinear boundary conditions can be satisfied on the instantaneous free water and body surfaces. The unknowns are distributed on the boundary of the whole computational domain, and a new linear equation system must be generated and solved at each time step, since the free surface (and the body surface if it is not fixed) move to new positions. Recent applications of this approach to simulate nonlinear wave diffraction include Ma et al. (2001a, b), Turnbull et al. (2003), and Wu and Hu (2004), who developed numerical wave tanks based on the finite element model. The alternative boundary element method was used by Contento (2000), and Koo and Kim (2004), for simulations in a two-dimensional wave

tank and by Ferrant et al. (2003) for three-dimensional simulations of the diffraction problem. In addition, Grilli et al. (2001) and Xue et al. (2001) used the higher-order boundary element method to investigate three-dimensional overturning waves in a numerical wave tank.

Early nonlinear investigations were focused on either the radiation problem alone, or the diffraction problem. The emphasis of much previous research on wave radiation problems has been on solving them in the frequency-domain. In the time domain, Isaacson and Ng (1993) investigated the second-order radiation problem for the forced motions of a truncated cylinder. Lee et al. (1994), and Wu and Eatock Taylor (1995), calculated the fully nonlinear wave radiation due to oscillations of a submerged sphere and a submerged circular cylinder respectively. Maiti and Sen (2001) have obtained the two-dimensional results for vertical structures undergoing forced motions, and Hu et al. (2002) calculated the radiated wave field around translating three-dimensional structures using the finite element method. Bai and Eatock Taylor (2006) calculated the radiated wave field around three-dimensional (3D) surface piercing structures. This work forms the initial stages of development of the nonlinear model OXPOT. To investigate the problem of fully nonlinear wave diffraction, Ma et al. (2001a, 2001b) developed a numerical wave tank based on the FEM. The alternative BEM was used by Boo (2002) and Ferrant et al. (2003). In an extension to OXPOT, Bai and Eatock Taylor (2007) performed simulations of three-dimensional wave diffraction.

Investigation of the fully nonlinear wave interactions with freely floating 3D structures requires the treatment of the coupling between hydrodynamic force and body motion. A highly accurate calculation of the wave force is therefore demanded. Direct evaluation of the force requires the time derivative of the potential, ϕ_t, which it is known can affect the stability of the entire computation when the body is free to move. Contento (2000) adopted numerical differencing of the total material derivative of the potential, and thereby obtained ϕ_t. Another method uses the acceleration potential method, as shown by Tanizawa (1996), and subsequently Koo and Kim (2004), where an additional equation for ϕ_t was solved. Wu and Eatock Taylor (1996) proposed an alternative method, in which some auxiliary functions were introduced and solved, in place of computing ϕ_t directly. The effectiveness of this method was demonstrated by Wu and Hu (2004) in their finite element simulation of three dimensional floating body responses.

A further extension to OXPOT is described by Bai and Eatock Taylor (2009). The paper describes a robust numerical model of submerged or surface-piercing three-dimensional bodies undergoing forced motions, such as surge, heave, pitch and their combination. The overall approach is as follows. Firstly, two coordinate systems are defined to describe the position of moving bodies, and the Mixed Eulerian-Lagrangian (MEL) technique is used to track the motion of a body which may have horizontal displacement. The higher-order boundary element method is adopted, which means that compared with other volume-discretised numerical methods such as the finite element method, remeshing is much easier, for example if the body motion has rotational components. Another advantage of using the higher-order boundary element method is that the calculation of the velocities of grid points, and the determination of the intersections of free water and solid surfaces, are more convenient. Against this, for cases where a large fluid domain must be simulated, the storage requirement of a boundary element model may well exceed that of an equivalent finite element model, as discussed by Wu and Eatock Taylor (2003). This disadvantage, however, may be overcome by the use of domain decomposition, as described by Bai and Eatock Taylor (2007) and discussed below. On the free water surface, unstructured triangular meshes are used, which have been found to be very suitable for complex geometries. In the case of strongly nonlinear waves, mesh regridding and interpolation techniques are employed on the free surface to mitigate numerical instability.

For the calculation of the hydrodynamic forces, some auxiliary functions are introduced, which lead to additional boundary value problems. The benefit of this technique is that it avoids the use of simple backwards time differencing schemes, which can lead to unexpected inaccuracy and instability.

Solution of the mixed boundary value problem for ϕ directly for N boundary element nodes requires $O(N^2)$ operations, which is prohibitive when N exceeds several thousand. Even if, as in OXPOT, the higher-order boundary element method is used, the computation of the three dimensional nonlinear simulation is still very demanding. As a result, previous investigations have often been restricted to small domains and short simulation times. Various attempts have been made to increase the computational efficiency, such as the Fast Multipole Method (e.g. Rokhlin, 1985, Fochesato and Dias, 2006) and the domain decomposition method. The latter approach has been implemented in OXPOT. This method has already been adopted in other research fields, for example in structural

dynamics (Farhat and Li, 2005), aeroacoustics (Arina and Falossi, 2004) and modelling explosions (Dean and Glowinski, 1999). In computational hydrodynamics, the domain decomposition method has received less attention: only Wang et al. (1995) and De Haas and Zandbergen (1996) appeared to have used this approach in a two dimensional implementation. It is particularly suitable for the parallel computing, as implemented for example by Cai et al. (2005) and Guo et al. (2006).

The basic idea of domain decomposition is to divide the computational region into many subdomains, and to apply the boundary element method to each individual subdomain, leading to far fewer unknowns in each subdomain compared with in the original region. Thus, the computational effort per subdomain is much reduced. The key issue in domain decomposition is to satisfy suitable continuity requirements between adjacent subdomains. This can lead to two alternative approaches. One is to define unknowns on both sides of the common surfaces between adjacent subdomains. Only one block-diagonalised coefficient matrix then needs to be assembled with contributions from all the subdomains (Wang et al., 1995). Another approach is to match the values of variables on the common surfaces through a suitable iteration procedure, with the assembly and solution of the coefficient matrix carried out in each independent subdomain (De Haas and Zandbergen, 1996). By contrast to the coefficient matrix in a volume-discretised approach, such as the finite element method, the submatrices arising from the first domain decomposition approach described above are full and unsymmetric, which makes the problem expensive to solve even though it is block-diagonalized. The second approach is more convenient to implement using parallel computing, because each processor can almost finish the computation in the corresponding subdomain independently of the information from other subdomains. We therefore use here the domain decomposition based on the iteration procedure, which generates a sequence of boundary conditions on the interfaces between the subdomains.

2.2 Mathematical formulation

To formulate the three-dimensional problem, a right-handed Cartesian coordinate system Oxyz having the origin O on the mean water surface and z-axis pointing vertically upwards is defined as shown in Fig. 1. Based on the potential flow theory, the wave-body interaction problem can be formulated in terms of a velocity potential $\phi(x, y, z, t)$, which satisfies Laplace's equation within the fluid domain Ω,

$$\nabla^2 \phi = 0\,, \tag{1}$$

and is also subject to various boundary conditions on all surfaces S of the fluid domain.

On the instantaneous free water surface SF, the kinematic and dynamic conditions in the Lagrangian description can be written as

$$\frac{\mathrm{D}\mathbf{X}}{\mathrm{D}t} = \nabla \phi\,, \tag{2}$$

$$\frac{\mathrm{D}\phi}{\mathrm{D}t} = -gz + \frac{1}{2}\nabla\phi \cdot \nabla\phi\,, \tag{3}$$

where D/Dt is the usual material derivative, X denotes the position of points on the free surface, and g is the acceleration due to gravity. The kinematic condition on the instantaneous wetted body surface SB is

$$\frac{\partial \phi}{\partial n} = \mathbf{V}_n\,, \tag{4}$$

where n is the normal unit vector pointing out of the fluid domain, and Vn the normal velocity component of the body surface. The motions of a three-dimensional rigid body about its centre of mass located at Xg=(xg, yg, zg) can be described in terms of six components, and then

$$\mathbf{V}_n = \left(\dot{\boldsymbol{\xi}} + \dot{\boldsymbol{\alpha}} \times \left(\mathbf{X} - \mathbf{X}_g \right) \right) \cdot \mathbf{n}\,, \tag{5}$$

where $\xi=(\xi_1, \xi_2, \xi_3)$ is a vector denoting the displacements of surge, sway and heave, while $\alpha=(\xi_4, \xi_5, \xi_6)$ is a vector indicating the angles of roll, pitch and yaw about X_g measured in the clockwise direction. We can regard the wave maker S_M as another body surface moving only in the x direction. The boundary condition on the fixed body surface can be reduced to the same form as that on the side wall SW and the horizontal seabed S_D, namely the impermeability condition

$$\frac{\partial \phi}{\partial n} = 0\,. \tag{6}$$

Since the problem is solved in the time domain, an initial condition must be imposed as well. In this formulation, the body starts from rest in calm water, so that the velocity potential and wave elevation can be set to

$$\phi = 0, \zeta = 0 \qquad t \le 0 . \tag{7}$$

In addition, a proper far field condition should be implemented to avoid the unwanted wave reflection from the downstream end of the domain; this will be discussed later.

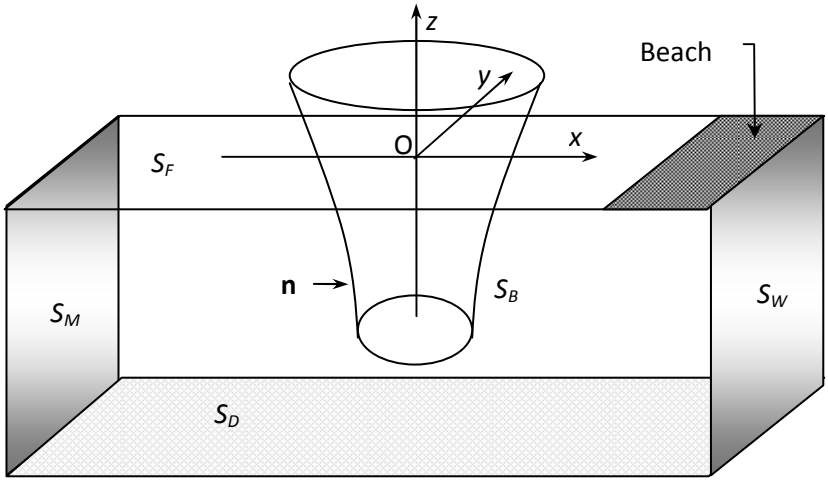

Fig. 1 Definition sketch

2.3 Higher-order boundary element simulation

The boundary element method is widely used to solve the mixed boundary value problem in the numerical simulation of nonlinear waves, because it can reduce the dimension of the problems to be solved by one. If a Rankine source is adopted as the Green's function *G*, a boundary integral equation for the potential ϕ over the whole boundary *S* can be derived, expressing the original potential flow problem through Green's second identity:

$$C(\mathbf{x}_0)\phi(\mathbf{x}_0) = \iint_S \left[G(\mathbf{x},\mathbf{x}_0)\frac{\partial\phi(\mathbf{x})}{\partial n} - \phi(\mathbf{x})\frac{\partial G(\mathbf{x},\mathbf{x}_0)}{\partial n} \right] ds . \tag{8}$$

Here $C(\mathbf{x}_0)$ is the solid angle at the field point $\mathbf{x}_0$, and **n** is measured from the source point **x**. For cases in which the body and the simulated flow are symmetric about the *x*-*z* plane, and the seabed is horizontal, the simple Rankine source and its image with respect to the symmetry plane ($y = 0$) and the seabed ($z = -d$) can be chosen as the Green's function. Thus, the integral only needs to be

evaluated over the half of the computational boundaries, and the seabed is excluded. Under these conditions, the Green's function can be written as

$$G(\mathbf{x},\mathbf{x}_0)=\frac{1}{4\pi}\left(\frac{1}{R_1}+\frac{1}{R_2}+\frac{1}{R_3}+\frac{1}{R_4}\right), \tag{9}$$

where

$$\begin{cases} R_1=\sqrt{(x-x_0)^2+(y-y_0)^2+(z-z_0)^2} \\ R_2=\sqrt{(x-x_0)^2+(y+y_0)^2+(z-z_0)^2} \\ R_3=\sqrt{(x-x_0)^2+(y-y_0)^2+(z+z_0+2d)^2} \\ R_4=\sqrt{(x-x_0)^2+(y+y_0)^2+(z+z_0+2d)^2} \end{cases}. \tag{10}$$

It is well known that the higher-order boundary element method is more efficient and accurate than the constant panel method. In this numerical method, the surface over which the integral is performed is discretised by quadratic isoparametric elements. Eight and six nodes are placed on curved quadrilateral and triangular elements respectively. After introducing shape functions $N_j(\xi, \eta)$ in each surface element, one can write the position coordinate, the velocity potential and its derivatives within an element in terms of nodal values, in the following forms:

$$\mathbf{x}(\xi,\eta)=\sum_{j=1}^{K}N_j(\xi,\eta)\mathbf{x}_j\ ;\quad \phi(\xi,\eta)=\sum_{j=1}^{K}N_j(\xi,\eta)\phi_j\ ; \tag{11}$$

$$\frac{\partial\phi(\xi,\eta)}{\partial\xi}=\sum_{j=1}^{K}\frac{\partial N_j(\xi,\eta)}{\partial\xi}\phi_j\ ;\quad \frac{\partial\phi(\xi,\eta)}{\partial\eta}=\sum_{j=1}^{K}\frac{\partial N_j(\xi,\eta)}{\partial\eta}\phi_j\ , \tag{12}$$

where K is the number of nodes in the element, $\mathbf{x}_j$ and ϕ_j are the nodal positions and potentials, and (ξ, η) are local intrinsic coordinates. By substituting these representations into Eq. (8), a boundary integral equation in discretised form can be rewritten as

$$C(\mathbf{x}_0)\phi(\mathbf{x}_0) = \sum_{n=1}^{N}\sum_{m=1}^{M}\left\{ G(\mathbf{x}_m,\mathbf{x}_0)\left[\sum_{j=1}^{K} N_j(\xi,\eta)\left(\frac{\partial\phi}{\partial n}\right)_j\right] - \frac{\partial G(\mathbf{x}_m,\mathbf{x}_0)}{\partial n}\left[\sum_{j=1}^{K} N_j(\xi,\eta)\phi_j\right]\right\} w_m \left|J_m(\xi,\eta)\right| , \tag{13}$$

where M is the number of sampling points used in the standard Gauss-Legendre method to evaluate numerically the integration over each element, w_m is the integral weight at the mth sampling point, $J_m(\xi, \eta)$ is the Jacobian transformation from the global to the local intrinsic coordinates, and N is the number of elements. At this stage, $\mathbf{x}_0$ is an arbitrary point on the free surface and other discretised boundaries. It is now specified to be one of the element nodes. When the field point is located at a node within a particular element, the associated singularity is evaluated by using the triangular polar-coordinate transformation technique described by Eatock Taylor and Chau (1992). At a given time step, either the potential or its normal derivative on each part of the boundary is known from the corresponding boundary conditions: the remaining unknowns can then be calculated by solving the above discretised equation.

We notice that the solid angle $C(\mathbf{x}_0)$ in Eq. (13) still needs to be determined, and it is difficult to compute directly for the complex evolving three-dimensional computational domain. However, the treatment of the solid angle can be simplified by using the physical argument that a uniform potential applied over a closed domain produces no flux. This is equivalent to considering a homogeneous Dirichlet problem, in which a uniform field, Φ = constant $\neq$ 0, is specified over the whole integral boundary S (Wu and Eatock Taylor, 1989). The boundary integral equation, Eq. (8), in such a case leads to

$$C(\mathbf{x}_0) = -\iint_S \frac{\partial G(\mathbf{x},\mathbf{x}_0)}{\partial n} ds \, . \tag{14}$$

This convenient formula expresses the solid angle as an integration of the derivative of the Green's function, which can be obtained directly from the influence coefficients without additional work.

Finally, the resulting discretised equation can be expressed in the matrix form:

$$\begin{bmatrix} \mathbf{A}^{(11)} & \mathbf{A}^{(12)} \\ \mathbf{A}^{(21)} & \mathbf{A}^{(22)} \end{bmatrix} \begin{Bmatrix} \mathbf{X}^{(1)} \\ \mathbf{X}^{(2)} \end{Bmatrix} = \begin{Bmatrix} \mathbf{B}^{(1)} \\ \mathbf{B}^{(2)} \end{Bmatrix}, \tag{15}$$

where

$$\mathbf{X}^{(1)} = \{\phi_1, \phi_2, \cdots, \phi_{N_n}\}; \quad \mathbf{X}^{(2)} = \left\{ \left(\frac{\partial \phi}{\partial n}\right)_1, \left(\frac{\partial \phi}{\partial n}\right)_2, \cdots, \left(\frac{\partial \phi}{\partial n}\right)_{N_p} \right\}; \tag{16}$$

$$A_{i,j}^{(11)} = C(\mathbf{x}_i) + A_{i,j}^{(21)}; \quad A_{i,j}^{(21)} = \sum_{n=1}^{N_n} \sum_{m=1}^{M} \left[\frac{\partial G(\mathbf{x}_m, \mathbf{x}_i)}{\partial n} N_j(\xi, \eta) w_m |J_m(\xi, \eta)| \right]; \tag{17}$$

$$A_{i,j}^{(12)} = A_{i,j}^{(22)} = -\sum_{n=1}^{N_p} \sum_{m=1}^{M} \left[G(\mathbf{x}_m, \mathbf{x}_i) N_j(\xi, \eta) w_m |J_m(\xi, \eta)| \right]; \tag{18}$$

$$\begin{aligned} B_i^{(1)} = & \sum_{n=1}^{N_n} \sum_{m=1}^{M} \left[G(\mathbf{x}_m, \mathbf{x}_i) \frac{\partial \phi(\mathbf{x}_m)}{\partial n} w_m |J_m(\xi, \eta)| \right] - \\ & \sum_{n=1}^{N_p} \sum_{m=1}^{M} \left[\frac{\partial G(\mathbf{x}_m, \mathbf{x}_i)}{\partial n} \phi(\mathbf{x}_m) w_m |J_m(\xi, \eta)| \right]; \quad B_i^{(2)} = -C(\mathbf{x}_i)\phi(\mathbf{x}_i) + B_i^{(1)}. \end{aligned} \tag{19}$$

Here, N_n and N_p are the numbers of elements on the Neumann and Dirichlet boundaries respectively. After assembling the equations for each node on the whole integral surface, a set of linear algebraic equation system is obtained, which can be solved to get the solution of the mixed boundary value problem described from Eq. (1) to Eq. (6) at a certain time step.

2.4 Hydrodynamic forces

Once the potential has been found by solving the mixed boundary value problem at each time step, the pressure on the body is expressible using the Bernoulli equation,

$$p = -\rho \left(\phi_t + \frac{1}{2} \nabla \phi \cdot \nabla \phi + gz \right), \tag{20}$$

where ρ is the density of the fluid. The hydrodynamic forces **F** = {f_1, f_2, f_3} and moments **M** = {f_4, f_5, f_6} can consequently be obtained by integrating the pressure over the wetted body surface,

$$f_i = \iint_{S_B} p n_i ds \qquad (i = 1,\ldots,6), \tag{21}$$

where n_i are the six components of the normal unit vector **n** defined in Eq. (4). The velocity components $\nabla\phi$ on the body surface in Eq. (20) may be obtained numerically. More difficult, however, is the evaluation of the time derivative, ϕ_t. Estimating this quantity by a simple backward difference scheme is inaccurate and prone to instabilities, particularly in the more general case when the body is free to move.

An effective method of calculating the hydrodynamic force is to solve a separate boundary value problem, as used by Wu and Eatock Taylor (1996). In this approach, some auxiliary functions ψ_i (i = 1,…,6) are introduced, in place of computing ϕ_t directly. These functions satisfy the Laplace equation in the fluid domain, and the following conditions on the corresponding boundary surfaces. On the free water surface we specify

$$\psi_i = 0; \tag{22}$$

the condition on the body surface is taken as

$$\frac{\partial \psi_i}{\partial n} = n_i; \tag{23}$$

and on other boundary surfaces, we use the Neumann condition

$$\frac{\partial \psi_i}{\partial n} = 0. \tag{24}$$

In order to obtain the hydrodynamic force through the auxiliary functions, a relationship between ψ_i and ϕ_t needs to be developed, based on Green's identity,

$$\iint_S \left(\phi_t \frac{\partial \psi_i}{\partial n} - \psi_i \frac{\partial \phi_t}{\partial n} \right) = 0. \tag{25}$$

Using the boundary conditions for ψ_i and ϕ_t, in conjunction with Stokes theorem applied on the body surfaces, the above equation can be simplified and finally gives the following expression for the hydrodynamic force (the details are given by Wu and Eatock Taylor, 2003)

$$f_i = -\rho \iint_{S_B+S_F} \left(gz + \frac{1}{2}\nabla\phi \cdot \nabla\phi \right) \frac{\partial \psi_i}{\partial n} ds - \rho \iint_{S_B} \psi_i \left(\dot{\boldsymbol{\xi}} - \dot{\boldsymbol{\alpha}} \times \left(\mathbf{X} - \mathbf{X}_g \right) \right) \cdot \mathbf{n} ds$$
$$+ \rho \iint_{S_B} \left\{ \nabla \psi_i \left[\left(\boldsymbol{\xi} - \boldsymbol{\alpha} \times \left(\mathbf{X} - \mathbf{X}_g \right) \right) \cdot \mathbf{n} \right] \cdot \left[\nabla \phi - \left(\boldsymbol{\xi} - \boldsymbol{\alpha} \times \left(\mathbf{X} - \mathbf{X}_g \right) \right) \right] \right.$$
$$\left. - \psi_i \left(\boldsymbol{\alpha} \times \boldsymbol{\xi} \right) \cdot \mathbf{n} \right\} ds \qquad (26)$$

The key to obtaining the hydrodynamic force is therefore to solve for ψ_i. It can be seen that this second mixed boundary value problem for ψ_i has the same conditions (Neumann or Dirichlet) on the same boundary surface as the first mixed boundary value problem for ϕ, which means these two different problems share the same influence coefficient matrix. Therefore, it does not take much additional computer time to calculate the hydrodynamic forces by using this auxiliary function method, compared with the backward difference scheme in time. Moreover, this method can be applied easily in the calculation of the wave interaction with freely moving structures without any additional difficulties, as has been shown in Wu and Eatock Taylor (2003).

2.5 Numerical implementation

In the application of the numerical method to simulate nonlinear water waves, a number of aspects related to the detailed performance have to be considered, which have a direct bearing on success or failure of the calculation. These are discussed next.

2.5.1 Mesh generation

Within OXPOT the boundary integral equations are discretised using quadratic boundary elements, based on Eqs. (15) - (19). Here we consider how the element mesh is established. First, we note that in general the whole domain boundary is not a smooth, continuous surface: there are many corners and edges, for example between the free surface and body surface. In order to deal with this, the discretised surface is divided into many simple, continuous patches, and the mesh generation is performed on each of them.

As a higher-order boundary element method is used, the field point $\mathbf{x}_0$ can be located at the corners or edges of the boundary surfaces and this will result in a singularity where the normal vectors at these points are undefined. To deal with this, a double or triple node is employed at the edges or corners. One can place two or three different nodes at one spatial position to represent the different normal vectors.

There are two main types of patches in the computational domain. One type is the patch on vertical surfaces including the side wall and the body surface, which is easy to generate with structured quadrilateral meshes. The corner nodes are distributed exponentially in the *z* direction with a view to approaching the vertical decay of the potential. Thus the coordinates are taken as

$$z_{i,j} = z_{1,j} - \left(z_{1,j} + D\right) \cdot \frac{1 - \exp\left[\gamma\left(z_{1,j} + D\right)\left(M_z + 1 - i\right)/M_z\right]}{1 - \exp\left[\gamma\left(z_{1,j} + D\right)\right]} \qquad \left(i = 1, \ldots, M_z + 1\right), \tag{27}$$

where $z_{1,j}$ is the coordinate of the point where the wave intersects the vertical surface, M_z is the number of elements in the *z* direction, and *D* is the water depth or the draft of the body. The choice of parameter γ in the equation depends on how fine the mesh is required to be near the free surface. Subsequently, the position of the middle nodes in each element is determined by averaging that of the two adjoining corner nodes.

Another type of patch involves the free surface, and the bottom of the body if it is truncated. For these surfaces, unstructured triangular meshes are adopted, which are particularly suited to discretising complex domain boundaries. To generate triangular meshes, the Delaunay triangulation method (Subramanian et al., 1994) is applied in the present work.

The generation of initial triangles is the first step in the Delaunay triangulation method, i.e. a series of points on the known computational boundaries are considered as vertices of Delaunay triangles. Based on this set of coarse Delaunay triangles, points can then be inserted in the domain to form finer triangles. In order to generate meshes automatically and blend the grid density smoothly from the boundaries to the interior domain, the circumcircle radius is used as a measure of the obtuseness of the element (which ideally should be as close as possible to equilateral). This variable is made dimensionless by a local length scale, which reflects the grid density on the boundaries influencing the local mesh. The automatic procedure can then be developed by specifying that a new node is placed at the centre of the triangle having maximum circumcircle radius. Finally, the Laplace smoothing method is used to smooth the meshes, such that their shape approaches regular triangles as much as possible. Fig. 2 shows meshes generated by this method for a truncated cylinder.

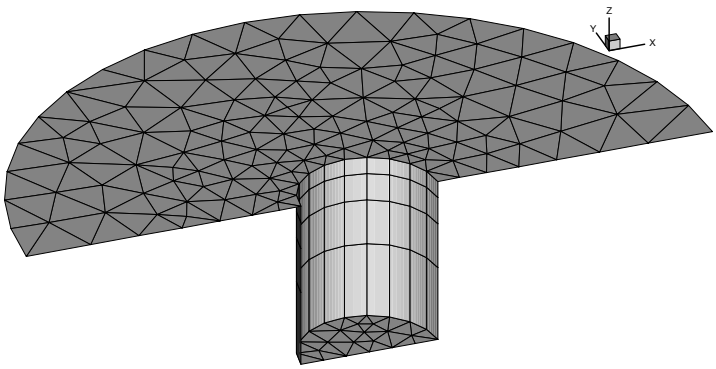

Fig. 2 An example mesh generated on the body and free water surfaces for illustration of the mesh generation

2.5.2 Artificial damping layer

In order to avoid the reflection of scattered waves from the far-field computational boundaries and to simulate a sufficiently long duration in a reasonably sized domain, it is necessary to impose a suitable radiation condition on the outer boundaries. Many forms of far field condition have been developed by other investigators. Here an artificial damping layer on the free surface is adopted to absorb the scattered wave energy on the outer annulus of a circular cylindrical domain. In this numerical beach, the kinematic and dynamic boundary conditions are modified by a damping term over a finite length of the free surface (Ferrant, 1993),

$$\frac{\mathrm{D}\mathbf{X}}{\mathrm{D}t} = \nabla\phi - \nu(r)\left(\mathbf{X} - \mathbf{X}_e\right), \tag{28}$$

$$\frac{\mathrm{D}\phi}{\mathrm{D}t} = -gz + \frac{1}{2}\nabla\phi\cdot\nabla\phi - \nu(r)\phi, \tag{29}$$

where r is the distance from the body, $\nu(r)$ is the damping coefficient, and $\mathbf{X}_e=(x_e, y_e, 0)$ is a reference value specifying the at-rest position of the fluid particle. In practice, the damping coefficient is chosen to be continuous and continuously differentiable, and is "tuned" to a characteristic excitation frequency ω of wave motion. Here we have used:

$$\nu(r) = \begin{cases} \alpha\omega\left(\dfrac{r - r_0}{\beta\lambda}\right)^2 & r \geq r_0 = r_D - \beta\lambda \\ 0 & r < r_0 \end{cases} . \tag{30}$$

In this definition, λ is a representative wavelength corresponding to the excitation, r_D is the radius of the outer circular computational domain, and the two non-dimensional parameters α and β are used to control the strength of damping layer and the length of beach respectively.

2.5.3 Time stepping integration

After solving the boundary value problem defined above, the free surface geometry and potential are updated for the calculation at the next time step, by integrating the fully nonlinear free surface boundary conditions in time, in an iterative manner. Here, the standard 4th-order Runge-Kutta scheme (RK4) is used, providing good stability characteristics within a convenient computational scheme.

Before the time stepping integration of the free surface boundary conditions, one first needs to compute the particle velocities. From the solutions of the mixed boundary value problem or the corresponding boundary conditions, the potential and its normal derivative on boundaries of the whole fluid domain are all known. Based on the higher-order boundary element method adopted here, the particle velocities both on the free water surface and body surface can be easily determined by use of the following formula:

$$\begin{bmatrix} \dfrac{\partial\phi}{\partial x} \\ \dfrac{\partial\phi}{\partial y} \\ \dfrac{\partial\phi}{\partial z} \end{bmatrix} = \begin{bmatrix} \dfrac{\partial x}{\partial\xi} & \dfrac{\partial y}{\partial\xi} & \dfrac{\partial z}{\partial\xi} \\ \dfrac{\partial x}{\partial\eta} & \dfrac{\partial y}{\partial\eta} & \dfrac{\partial z}{\partial\eta} \\ n_x & n_y & n_z \end{bmatrix}^{-1} \begin{bmatrix} \dfrac{\partial\phi}{\partial\xi} \\ \dfrac{\partial\phi}{\partial\eta} \\ \dfrac{\partial\phi}{\partial n} \end{bmatrix} . \tag{31}$$

It should be noted that there is always more than one element surrounding a node. The final velocity at each node is thus obtained by averaging the values from Eq. (31) performed within every element adjacent to this node. Where the surface is discontinuous, it is divided into smooth and continuous patches, and the multiple node method is used on the interfaces between these patches. The same

averaging procedure stated above can then be adopted to predict the velocity and the normal vector at the multiple nodes, but in this situation only the surrounding elements located on the same patch as the node should be considered in the averaging. In this way, the flow in the domain at the advanced time $t+\Delta t$ can be solved, and the time domain calculation can proceed.

During the initial time steps, an abrupt initial condition should be avoided, and a cosine ramp function F_m can be used to modulate the wavemaker motion. F_m is taken as

$$F_m = \begin{cases} \frac{1}{2}\left[1-\cos\left(\frac{\pi t}{T_m}\right)\right] & t < T_m \\ 1 & t \geq T_m \end{cases}. \tag{32}$$

where T_m is a ramp time, chosen as two times the excitation period T in the case of regular waves.

2.5.4 Algebraic equation solver

The solution of the full and asymmetric influence matrix arising from the mixed boundary value problem at each time step is a significant part of the calculation. The efficient generalized minimum residual (GMRES) iterative scheme with a diagonal preconditioner is used in the present work, which was first proposed by Saad and Schultz (1986), and applied in the ocean engineering field by Zhao and Graham (1996). We have found this solver to be very effective.

At the same time, when assembling the influence matrix, one should notice that on the intersection of the free surface and the solid surfaces, the potential on the free surface is known from the free surface boundary condition, and therefore the potential of the double or triple nodes on the solid surfaces is also known according to the continuity of potential. Therefore, there are no unknown variables on the double or triple nodes belonging to the solid surfaces, and the corresponding terms can be moved to the right-hand side of the equation. Here for the node designated k, Eq. (15) can be changed to

$$\begin{cases} B_k = \phi_k; & B_i\big|_{i\neq k} = B_i - A_{i,k}\phi_k \\ A_{k,k} = 1; & A_{k,j}\big|_{k\neq j} = A_{i,k}\big|_{i\neq k} = 0 \end{cases}. \tag{33}$$

2.5.5 Mesh regridding

The integration of free surface boundary conditions in time will update the wave profile and the intersection lines of the free surface and solid boundaries, which means the meshes on these boundaries have to be adjusted accordingly. In addition, for the case of an oscillating body, its motion may require re-calculation of the positions of nodes on the body surface.

On the vertical side walls of the tank, the mesh regridding is simple, similar to that at the initial time step discussed above, because $z_{1,j}$ in Eq. (27) is the only variable changing its value during the free surface update. In order to illustrate the mesh regridding on the body surface, we can consider its motion to involve only three components, surge, heave and pitch, defined as (χ_1, χ_3, χ_5). In such a case, the *y* coordinate need not be considered in the mesh regeneration. We recall that two coordinate systems have been defined, and so we need to transform the positions of nodes from the moving body-fixed coordinates to the space-fixed coordinates. In matrix form the transformation can be written as

$$\begin{bmatrix} x \\ z \end{bmatrix} = \begin{bmatrix} x_g + \chi_1 \\ z_g + \chi_3 \end{bmatrix} + \begin{bmatrix} \cos\chi_5 & -\sin\chi_5 \\ \sin\chi_5 & \cos\chi_5 \end{bmatrix} \begin{bmatrix} x' \\ z' \end{bmatrix}. \tag{34}$$

Under most conditions without regridding, the numerically computed wave profile will, after a sufficiently long time, develop a saw-tooth appearance. Remeshing on the free surface, as implemented here, can remove this numerical instability. This approach avoids the arbitrariness of having to choose an explicit smoothing formula. To realize the mesh regeneration on the free surface, the following interpolation technique is used to predict the vertical coordinate of the new node based on its given horizontal coordinates. For boundary-fixed problems, the horizontal coordinate is computed at the initial time step, and then can be used at the following time steps. However, for many moving boundary problems, we need to move the nodes horizontally prior to the vertical interpolation, in order to maintain a uniform distribution of nodes and good aspect ratios for the elements.

This process is achieved by first discretizing the boundary line of the free surface projected onto the horizontal plane. For the part of this boundary line lying on the side walls, the discretization is direct because the horizontal coordinate is independent on the vertical coordinate. On the body surface, however, the horizontal and vertical coordinates are coupled, as seen in Eq. (34). Consequently, an iterative program is developed based on the new position of nodes obtained from the time stepping

integration, in order to ensure that the new node is located on the boundary line and the body surface. Once the new nodes on the boundary line of the free surface are known, the Laplacian smoothing technique is used to obtain the other new nodes on the free surface, *i.e.*:

$$(x,y)_i = \frac{1}{P}\sum_{j=1}^{P}(x,y)_j, \tag{35}$$

where P is the total number of nodes located around the node i.

2.5.6 Interpolation

Based on the horizontal coordinates of new nodes on the free water surface obtained by the mesh regeneration, interpolation can be employed to calculate the vertical position as well as the potential. In the interpolation, one must first find which old free surface element each new node belongs to, because when the fluid domain is remeshed, the new node cannot automatically be attached to a particular old element. To find the corresponding old element, the following criterion is used:

$$\sum_{k=1}^{Q} S_{sub}^{k} = S_{ele}, \tag{36}$$

where S_{sub} is the area of a triangular sub-element consisting of two vertices of the old element and the considered new node, S_{ele} is the area of the old element, and Q is the number of triangular sub-elements surrounding the node. If the equation is satisfied, the node must lie inside this element. The following numerical integration is used to calculate the area of a triangular element:

$$S = \sum_{m=1}^{M} w_m \left| J_m(\xi,\eta) \right|. \tag{37}$$

Finally the local intrinsic coordinates (ξ, η) can be determined based on the areas of sub-elements and the old element, and the vertical coordinate and potential at the new node can subsequently be obtained by using the shape function within this old element.

2.5.7 Intersection line

The intersections between the free water surface and the solid boundaries, such as the side walls and fixed or floating bodies, define sharp edges and corners on the domain boundary. At each time

step, the time integration of the free surface boundary conditions gives the new positions of nodes on the free surface. Also, due to the higher-order boundary element method used here, the intersections with the free surface can be calculated directly because the nodes are defined at the edges of each quadratic triangular element, unlike in the constant panel method where extrapolation is needed to determine the position of intersections.

There remains the possibility that the nodes on the intersection obtained by updating the free surface boundary conditions can separate from the body surface, due to numerical errors even though the separation is always very small. In order to fix the intersection, therefore, we simply force the double or triple nodes on the free surface back onto the body surface along its normal. By doing this, the intersections remain on the body surface exactly.

2.5.8 Domain decomposition

We now consider the computational domain Ω with prescribed boundary conditions to be decomposed into the subdomains Ω_1 and Ω_2, which are separated by an interface Γ. On the interface, the potential and its normal derivative are not known *a priori*, and an initial guess of Dirichlet condition $\phi^{(0)}$ or Neumann condition $\partial\phi^{(0)}/\partial n$ needs to be imposed. If ϕ equals the exact solution of the Laplace's equation in the original domain on the interface location, then the normal derivatives of the potential $\partial\phi_1/\partial n_1$ and $\partial\phi_2/\partial n_2$ in domains 1 and 2 will be continuous because of the uniqueness of the Laplace's equation. In the same way, the exact solution of $\partial\phi/\partial n$ on the interface will lead to a continuous potential over the interface. Therefore, the stop criterion on the interface for convergence of the iterative solution can be written as

$$\begin{cases} \left|\phi_1(\mathbf{x}) - \phi_2(\mathbf{x})\right| < \varepsilon_\phi \\ \left|\dfrac{\partial\phi_1}{\partial n_1}(\mathbf{x}) + \dfrac{\partial\phi_2}{\partial n_2}(\mathbf{x})\right| < \varepsilon_n \end{cases}, \tag{38}$$

where ε_ϕ and ε_n are the tolerances corresponding to ϕ and $\partial\phi/\partial n$, and n_1 and n_2 point out of domains 1 and 2 respectively.

There are different ways to construct the iteration sequence finding the exact value of ϕ and $\partial\phi/\partial n$ on the interface and the procedure used here is the following scheme, referred to as the D/D-N/N scheme (De Haas and Zandbergen, 1996):

0. Choose an initial Dirichlet condition $\phi^{(k)}$, (k=0).
1. Solve the Laplace's equation in Ω_1 and Ω_2 with the Dirichlet condition $\phi_1^{(k)}= \phi_2^{(k)}= \phi^{(k)}$ on Γ. This yields $\partial\phi_1^{(k)}/\partial n_1$ and $\partial\phi_2^{(k)}/\partial n_2$ on Γ.
2. Formulate a Neumann condition $\partial\phi^{(k+1)}/\partial n$ by taking an average of the computed solutions,

$$\frac{\partial\phi^{(k+1)}}{\partial n}=\frac{1}{2}\left(\frac{\partial\phi_1^{(k)}}{\partial n_1}-\frac{\partial\phi_2^{(k)}}{\partial n_2}\right). \tag{39}$$

3. Solve Laplace's equation with the Neumann condition $\frac{\partial\phi_1^{(k+1)}}{\partial n_1}=-\frac{\partial\phi_2^{(k+1)}}{\partial n_2}=\frac{\partial\phi^{(k+1)}}{\partial n}$ on Γ. This yields $\phi_1^{(k+1)}$ and $\phi_2^{(k+1)}$ on Γ.
4. Formulate a Dirichlet condition $\phi^{(k+2)}$ by taking an average of the computed solutions,

$$\phi^{(k+2)}=\frac{1}{2}\left(\phi_1^{(k+1)}+\phi_2^{(k+1)}\right). \tag{40}$$

5. Calculate the maximum error $\varepsilon^{(k+2)}$ on Γ, based on the potential obtained in Ω_1 and Ω_2,

$$\varepsilon^{(k+2)}=\max\left|\phi_1^{(k+1)}-\phi_2^{(k+1)}\right|. \tag{41}$$

6. If $\varepsilon^{(k+2)}$ satisfies the prescribed stop criterion, then exit the loop, and the final approximate solutions on the interface are $\phi^{(k+2)}$ and $\partial\phi^{(k+1)}/\partial n$.
7. Go to step 1 and repeat the procedure with k=k+2.

In the case of more subdomains the scheme can be extended straightforwardly by performing each step in the scheme on all subdomains and for all interfaces simultaneously.

In the numerical approach the Laplace equations are solved with the boundary element method in all subdomains separately. Bearing in mind the resources required by the boundary element method, the following implications with respect to storage and efficiency can be given:

- By introducing the interfaces, extra boundary elements and nodes are needed. However, because the memory required per subdomain depends quadratically on the number of nodes in the considered subdomain, the total required memory can be reduced considerably, depending on the number of interfaces.
- A similar comment may be made in relation to the computation time required to assemble the coefficient matrix, which only needs to be determined at the beginning of the iterative

procedure, since the geometry does not change during the iteration.

- There is a similar reduction of the required computation time for solving the linear algebraic system at each iteration step.

At the same time, it is important to note that we only generate a sequence of boundary conditions on the interfaces and that the conditions on the outer boundaries are fixed during the iteration process.

2.5.9 Singularity on interfaces

In the D/D-N/N scheme discussed above, we need to solve Laplace's equation in each subdomain with the Dirichlet and Neumann conditions on the interfaces at alternate iterative steps. On the free surface another Dirichlet condition is specified. Therefore, a problem appears on the intersection line between the free surface and the interface, where some double nodes are distributed. Because these double nodes share the same position and the same type of boundary condition, their coefficients obtained by Eq. (18) will be exactly the same: this will result in a singular algebraic equation system. To deal with this difficulty, semi-discontinuous elements are used in OXPOT.

Before explaining the semi-discontinuous element approach, we review the functions of the nodes within each boundary element. They can serve three purposes. Firstly, they define the shape of the boundary element. Secondly, they are used to specify the unknowns within each boundary element. Thirdly, they are used as collocation points. We can consequently consider three separate sets of nodes named according to their function as geometric nodes, functional nodes and collocation nodes respectively. In the present semi-discontinuous element approach, the geometric nodes and functional nodes are coincident but are staggered from the collocation nodes in order to avoid singular matrices. The collocation nodes are placed inside elements, while the geometric nodes and functional nodes are still located on the edges of elements. As a result Eq. (18) will yield different coefficients due to the different positions of the collocation nodes $\mathbf{x}_i$.

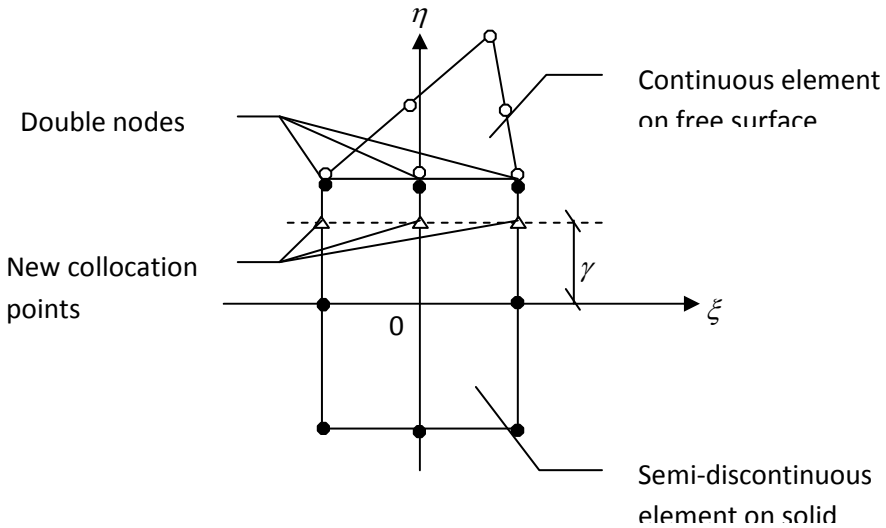

Fig. 3 The definition of the semi-discontinuous element

To specify the positions of the new collocation nodes, we define a discontinuity coefficient γ in the frame of the local intrinsic coordinates, as shown in Fig. 3. The range of this coefficient is from 0 to 1, and the discontinuous element would become continuous if γ=1. From the figure, we also note that the semi-discontinuous element approach is only adopted in elements located at the interfaces and adjacent to the free surface, and on the free surface the normal continuous elements are used. Moreover, the staggered collocation nodes only replace the three double nodes on one side of each quadrilateral semi-discontinuous element; this is the reason why the elements here are called “semi-discontinuous”. A similar semi-discontinuous boundary element method has also been used by Subia et al. (1995) and Guzina et al. (2006) for different problems. In their approaches, the functional and collocation nodes were coincident but were staggered from the geometric nodes. It can be noted that in our method the collocation nodes are located at different places from the functional nodes, as mentioned above; this avoids using different shape functions within the semi-discontinuous elements.

Once the positions of the new collocation nodes $\mathbf{x}_i$ are known, the coefficients in Eqs. (17), (18) and (19) can be determined. The known value $\phi(\mathbf{x}_i)$ in Eq. (19) also needs to be changed: it should be taken as the value on the new position of the collocation point, obtained by use of the shape functions. Another modification is the calculation of the singular integration, where the triangular

polar-coordinate transformation (Eatock Taylor and Chau, 1992) should be performed on the new sub-triangles defined by the new collocation points.

In the present method, structured quadrilateral meshes are adopted on the vertical solid surfaces, and unstructured triangular meshes are generated on the free surface by using the Delaunay triangulation method. A double or triple node is employed on the intersections between the free surface and vertical surfaces. Fig. 4 shows meshes generated by this method for a fixed vertical circular cylinder in a wave tank, in which three subdomains are involved.

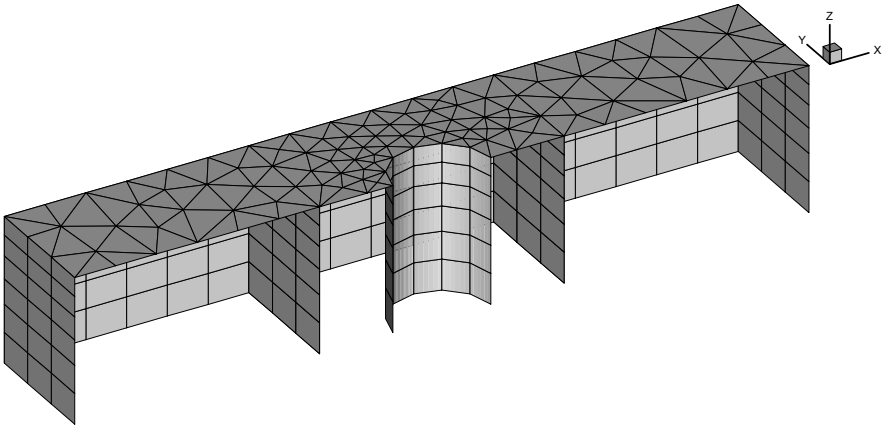

Fig. 4 An example mesh generated in a wave tank for illustration of the mesh generation

In order to avoid numerical instability, mesh regeneration on the free surface is used, leading to the need to specify the horizontal coordinates of the new nodes. Interpolation is then used to predict the vertical coordinate, and the potential at the new node. It should be noted that in the domain decomposition approach, this horizontal mesh regridding should not be applied just within each subdomain independently, as this would result in a bad distribution of elements over the interfaces (no information being transferred in that case between adjacent subdomains). We need to treat the free surface as a whole, and apply the Laplacian smoothing technique on the whole free surface.

The solution of the full and asymmetric influence matrix arising from the mixed boundary value problem at each time step is a significant part of the calculation. In general, the semi-discontinuous element approach provides slightly better conditioned matrix equations, but the convergence is still very slow when using an iterative scheme, such as the GMRES procedure. Therefore, the LU

decomposition method is used in conjunction with the domain decomposition approach. As the number of unknowns is small in each subdomain, the computational effort is not very large using this method. Because the coefficient matrix only depends on the geometry that is unchanged in the iterative process, there are only two types of coefficient matrix, corresponding to the problems with Neumann and Dirichlet boundary conditions respectively. We can compute the matrix factorisations once, which can be used on all odd and even steps of the iterative process, and then use the back substitution afterwards.

2.6 Discussion of model capabilities

The model OXPOT solves for the hydrodynamic interaction of waves with fixed or floating structures. The publications by Bai and Eatock Taylor (2006, 2007, 2009) and Eatock Taylor et al (2008) describe results which have been obtained with the model. These include nonlinear diffraction by fixed structures in regular waves and focused wave groups; nonlinear radiation by bodies oscillated sinusoidally by external forcing and bodies excited with prescribed transient motions; and the behaviour of freely floating bodies excited by a sinusoidal wavemaker in a numerical wave tank. Results have been obtained for hydrodynamic forces, body motions and wave elevation on the body waterlines. Cases considered in these publications include both wall-sided bodies and bodies with flare. Section 3 of this report summarises a few key cases and comparisons with other data.

Like other Computational Fluid Dynamics tools which involve time-stepping and regridding as the flow evolves, OXPOT requires substantial computational time to solve complex problems. One possibility for making substantial improvements to the efficiency of the technique described above would be to incorporate the use of a multipole solver (e.g. Nishimura, 2002, Liu and Nishimura 2006, Shen and Liu 2007). Another area of possible enhancement of the methodology would be to extend the range of conditions over which the model may be successfully used to obtain converged results. It is well known that nonlinear potential flow models of free surface flow are prone to numerical instabilities when used under conditions where strong motions arise, particularly in regions close to the body. As discussed in section 3.3 this is especially likely to be problematical for bodies with flare, in steep waves or when excited into large motion amplitudes. The first of these issues, efficiency, is relevant to the PerAWaT investigations, but flared structures are not expected to be considered in the programme. Both issues are being addressed in another nonlinear hydrodynamics project running at Oxford alongside PerAWaT. It is possible that the other project may yield improvements to the methodology, for example resulting in improved efficiency, which will result in an improved

version of OXPOT. The resulting improved OXPOT tool could then be used within PerAWaT to facilitate the extension of the range of cases investigated and longer data sets of results in irregular waves.

3. Illustrative results from OXPOT

3.1 Interaction of an impulse wave with a bottom-mounted circular cylinder

The first example concerns an asymmetric initial wave in a circular cylindrical tank with a surface-piercing cylinder at its centre. This can test the ability of the present numerical model to simulate the nonlinear wave patterns around the inner cylinder, and the calculation of the resulting horizontal wave force. In this case, the combination of incident, reflected and diffracted waves leads to rather complex free surface behavior. Chern et al. (2001) have also studied this case, using a pseudo-spectral matrix element method (PSME) to discretize the fully nonlinear free surface problem. The formula for the initial wave profile is defined as:

$$z(t=0) = a\exp\left[-\left(x-\frac{r+r_D}{2}\right)^2 - y^2\right]. \tag{42}$$

where r and r_D are the radius of the inner cylinder and the outer cylindrical wall, taken here as 1 and 10 respectively, and a is the amplitude of the initial wave profile, equal to 0.1. The peak of the impulse wave is located half way along the radial line between the walls of the inner and outer cylinders. In this case, mesh regeneration and interpolation on the free surface are not needed.

We first examine the convergence of the computation with three different meshes, chosen as shown in Table 1. The value of γ defining the mesh stretching in Eq. (27) is here taken as 1.0, and the time step is 0.1 unless otherwise specified. Figures 5(a) and 5(b) show the time history of wave elevation at the front of the cylinder, and the horizontal force on the cylinder with these three meshes respectively. It can be seen that the computation converges fast, and the results obtained with *mesh b* are very close to those obtained with *mesh c*. The wave force is seen to converge even faster than the wave elevation, most probably because the calculation of wave force is an integral over the wetted body surface.

Table 1. Numbers of elements and nodes for different meshes.

	Elements on body surface (circumferential×vertical)	Elements on side wall (circumferential ×vertical)	Elements on water surface	Nodes in whole domain
Mesh a	16×6	48×6	664	2672
Mesh b	24×6	72×6	1096	4208
Mesh c	32×6	96×6	1528	5744

The convergence of these numerical results with different time steps and the comparison with the results of Chern et al. (2001) is shown in Figure 6. From this figure, we cannot distinguish the difference between the results obtained at Δ*t*=0.1 and Δ*t*=0.05 with *mesh c*, and the present results agree well with those in Chern et al. (2001). Figure 7 compares free surface contours from these two numerical methods at two time instants, *t* = 15 and 30 respectively with *mesh c*. We can see that the agreement is basically satisfactory. However, in front of the inner cylinder some small differences can be noted when the free surface elevation is small, because the asymmetric unstructured meshes on the free surface we used are much coarser than the discretization in Chern et al. (2001).

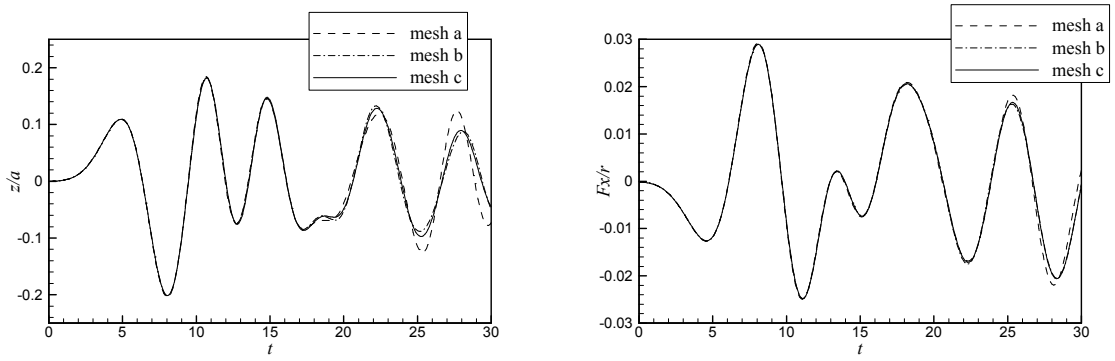

(a) (b)

Fig. 5 Convergence of the time history of wave elevation at front of cylinder and horizontal force on cylinder with different meshes: (a) wave elevation; (b) horizontal force

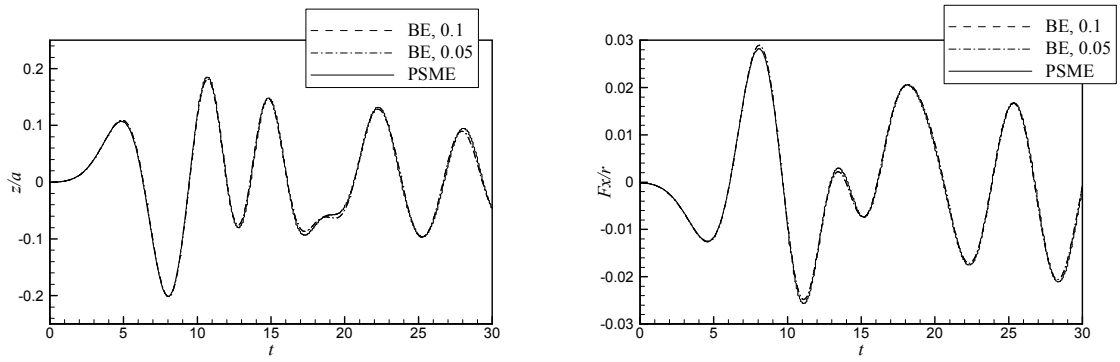

(a) (b)

Fig. 6 Comparison and convergence of the time history of wave elevation at front of cylinder and horizontal force on cylinder with different time steps: (a) wave elevation; (b) horizontal force

3.2 Propagation of regular waves in a rectangular tank

The efficiency of the artificial damping layer (Bai and Eatock Taylor, 2006) in absorbing reflected waves in a rectangular tank has been investigated by Bai and Eatock Taylor(2007). An example of the comparison of the wave profiles at two time instants in short and long tanks is shown in Fig. 7. We can see that the results are in good agreement, which indicates that there are no obvious waves reflected from the far end of the computational domain. It also can be seen how the propagating wave decays in the damping zone. The corresponding time history of the wave elevation at x=-3.12 is shown in Fig. 8. These figures confirm that the artificial damping layer works well.

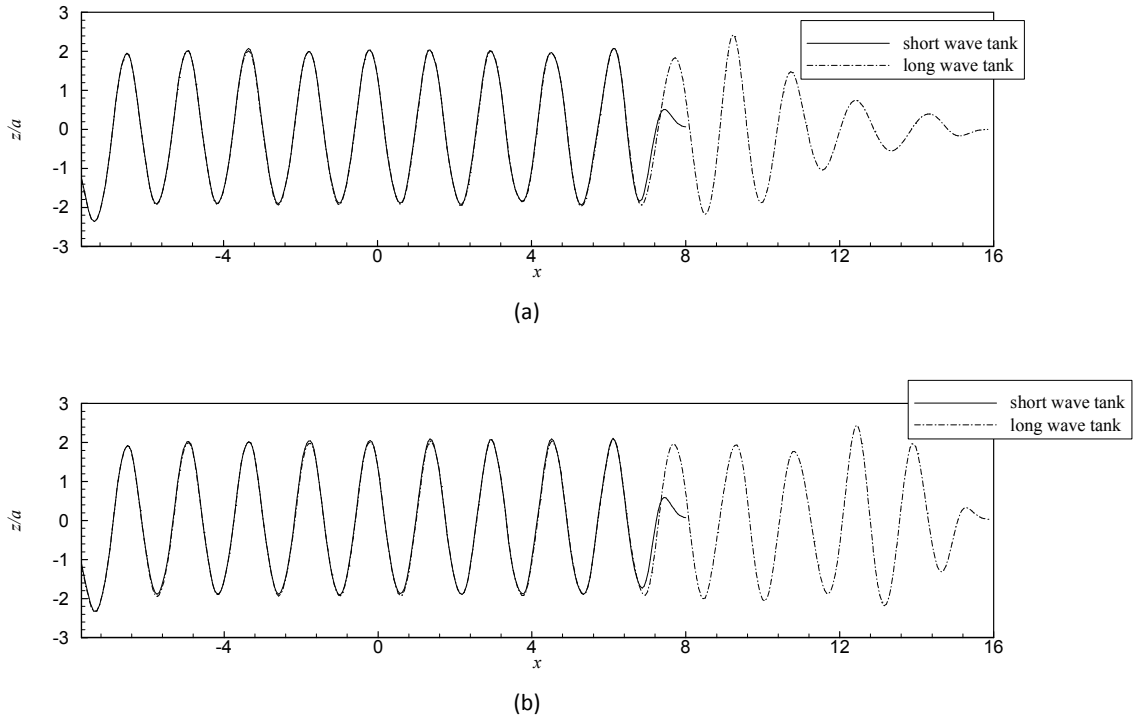

Fig. 7 Comparison of the wave profile in tanks of different length: (a) t=25T; (b) t=30T

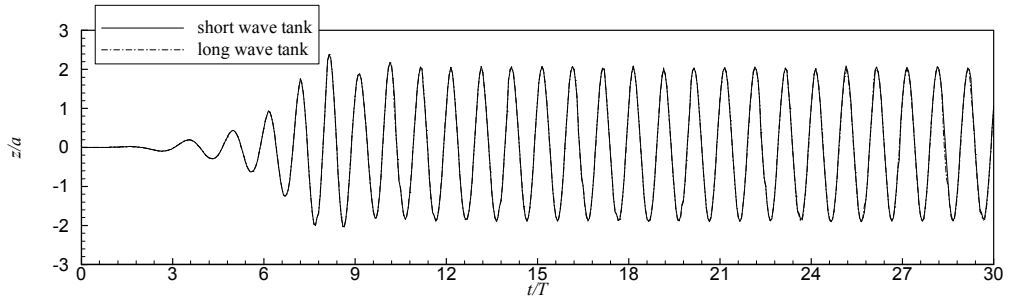

Fig. 8 Comparison of the wave elevation at x=-3.12 in tanks of different length

3.3 Focused wave in a wave tank

Focused wave groups were investigated by Bai and Eatock Taylor(2007) to verify the ability and accuracy of the present method. The numerical simulations reproduce the experiment made by Baldock et al. (1996), in which highly nonlinear wave-wave interactions were described. The wave

tank was 20 m long, 0.3m wide and had a maximum working depth of 0.7m. These authors assumed that the focus position is located at x=0, and the focus time is t=0. A linear wave solution then gives the required surface elevation generated at the wave maker as

$$\eta(x_P, t) = \sum_{n=1}^{N} A_n \cos\left(k_n x_P - \omega_n t\right), \tag{43}$$

where N is the total number of wave components, A_n, k_n and ω_n are the amplitude, wave number and wave frequency of the nth wave component respectively, and x_P is the position of the wave maker according to the linear prediction. From this equation, we obtain the linear wave amplitude at the focus position as $A = \sum_{n=1}^{N} A_n$.

A piston-like paddle was used as the wave maker. The relationship between the input signal and the resulting surface elevation, which affects the generation of a desired wave group, can be defined by a first order transfer function $T(a, \omega)$, such that

$$A(\omega) = T(a, \omega) a(\omega) . \tag{44}$$

Here $A(\omega)$ is the amplitude of the surface profile measured at the focus position, and $a(\omega)$ represents the amplitude of the sinusoidal input signal at a wave frequency ω. Baldock et al. (1996) determined this transfer function experimentally using an appropriate range of regular wave trains, in order to avoid the uncertainty associated with a theoretical prediction. In the present simulations, the transfer function was obtained numerically. By simulating regular waves with five different wave periods T in the range 0.6 to 1.4, for three different amplitudes of the input signal a, the influence of the wave amplitude on the transfer function was established. The calculations were performed in a wave tank which is 10λ long, 0.2λ wide and with a depth of 0.7m. Fig. 9 shows the resulting transfer functions, which were found to be insensitive to wave amplitudes in this range. This makes it possible to find a single curve-fit for the points in the figure, facilitating the generation of other desired waves by simple interpolation.

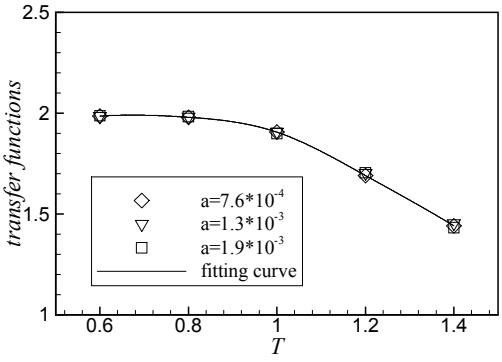

Fig. 9 Transfer functions for different motion amplitudes of the wave maker

Bai and Eatock Taylor (2007) simulated the focused waves identified as cases B and D in the experiment by Baldock et al. (1996). Case B is a wave group with a broad-band spectrum in which the wave periods range from 0.6 to 1.4s; while Case D is a wave group with a narrow-band spectrum in which the wave periods range from 0.8 to 1.2s. Each group consists of 29 individual wave components, which are of equal amplitude, and equally spaced within the appropriate period range. Because we are only interested in the wave surface near the focal point around the focal time, a smaller tank is adopted here compared with that in the experiment. The typical wave frequency and wave length used in the damping zone are chosen as the mean value and the maximum value of all wave components respectively. Twelve subdomains were applied, and remeshing was not needed.

Some typical results from Bai and Eatock Taylor (2007) are now discussed. Figs. 10 and 11 show the time histories of the surface elevation at the focal point for Cases B and D with three different input wave amplitudes (A=22mm, 38mm, and 55mm). As the hypothetical focused wave is assumed to be the linear sum of the individual wave components, it omits the effect of nonlinear wave-wave interactions. As a result, both the focal point and the focal time in the simulation and in the physical experiment are initially unknown. In the experiment, the focus position was determined experimentally for each wave group. In our numerical calculations, the focal time and focal position were predicted as follows. Around the expected linear focus time, we output the surface profile at many time instants. By comparing these, the position of the maximum wave elevation can be found, which is regarded as the focus point, with an associated focus time. However, the mesh on the free surface moves at every time step, which makes it difficult to specify the time history of the wave

elevation exactly at this focal point. Therefore, we also output the time history of the wave elevation at several nodes around the expected linear focal point, and obtain the final results using interpolation. It should be noted that in the figures shown below, both the focal position and the focal time are shifted to zero, in order to compare with linear predictions.

From Figs. 10 and 11, we can see that with the smallest input amplitude, the numerical results for both Case B and Case D agree well with the linear solution, confirming that the nonlinearity is very weak in this case. As the input amplitude is increased, the numerical results diverge from the linear solution gradually. The wave crest at the focal position is larger and narrower, while the wave troughs are wider and less deep, due to the stronger nonlinear interactions between wave components. The present numerical results are also very close to those in the experiment (Fig. 5 and 6 in Baldock et al., 1996), except in Case D with the highest input amplitude. In Fig. 11(c), the wave trough in the numerical results is deeper than that in the experiment.

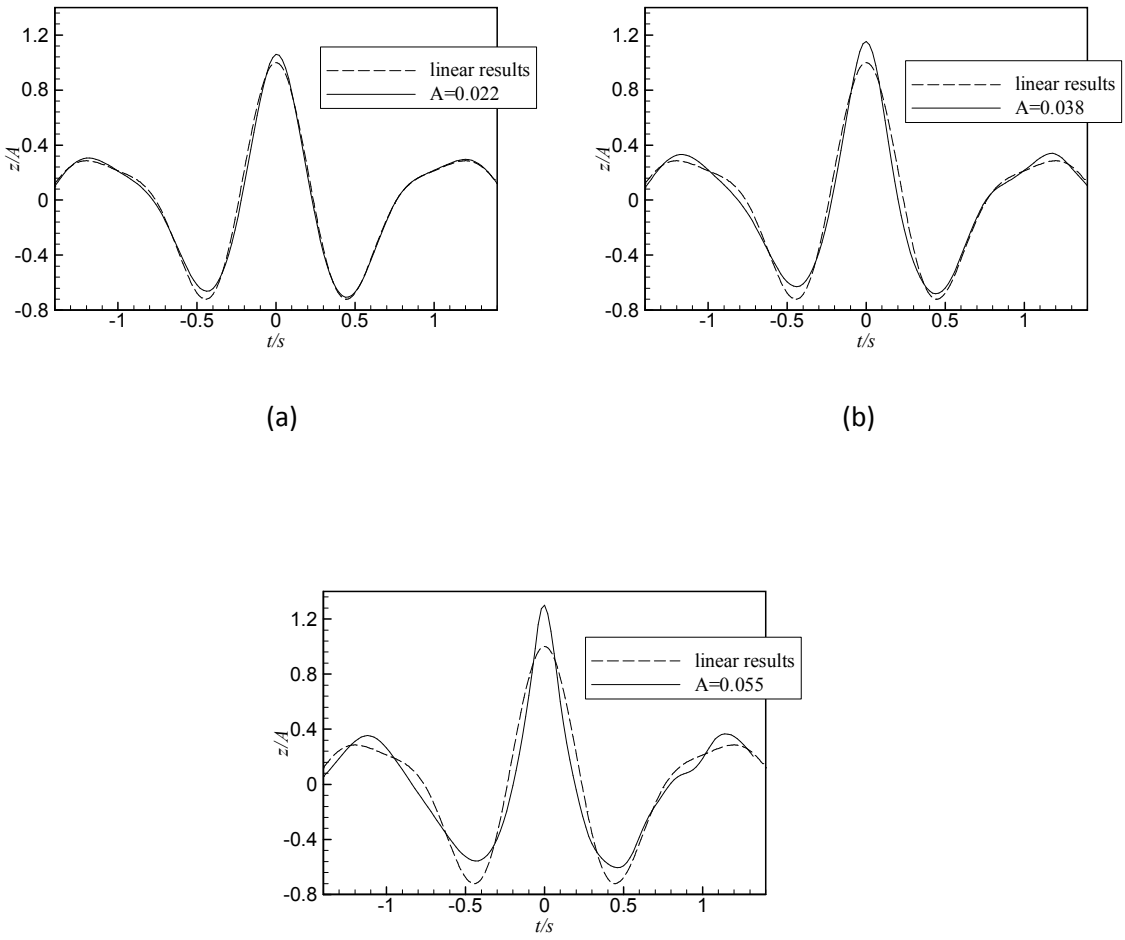

Fig. 10 Time history of the surface profile at the focal point for Case B: (a) *A*=0.022m; (b) *A*=0.038m; (c) *A*=0.055m (from Bai and Eatock Taylor, 2007)

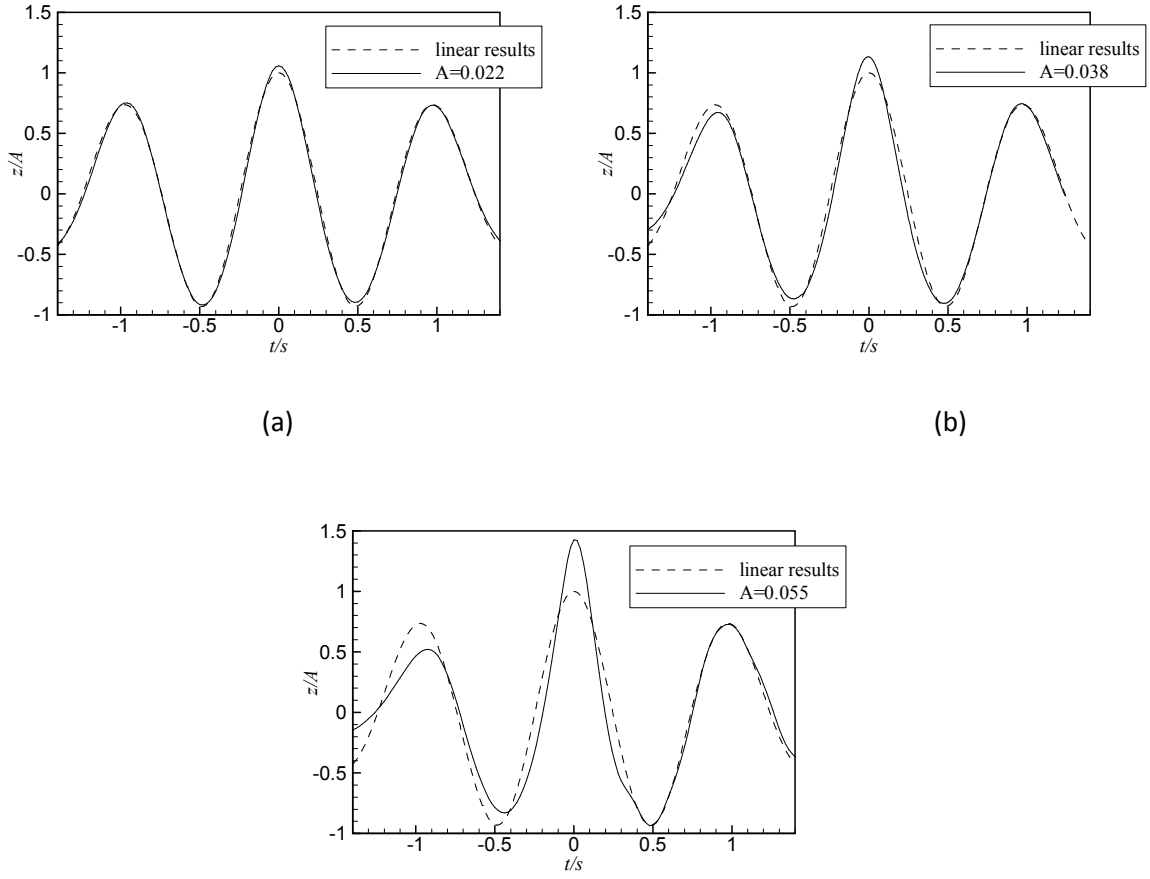

Fig. 11 Time history of the surface profile at the focal point for Case D: (a) *A*=0.022m; (b) *A*=0.038m; (c) *A*=0.055m (from Bai and Eatock Taylor, 2007)

Fig. 12 showing the maximum crest elevations at the focal point for different input amplitudes confirms again that the focusing of wave components produces a highly nonlinear wave group in which the nonlinearity increases with the input wave amplitude and reduces with increasing bandwidth. Based on the results obtained for Case B and Case D, the shifts of focal position and focal time due to nonlinear effects are shown in Fig. 13. The downstream shift of the focus point can be seen clearly in Fig. (13a), becoming larger with the increase of the input wave amplitude. The occurrence of the focusing event is increasingly delayed as the nonlinearity of the wave group increases. We find from the comparison with the results in the experiment, that the present numerical estimates of the focal position and the focal time are somewhat under-predicted at the

highest input wave amplitude, especially for Case D.

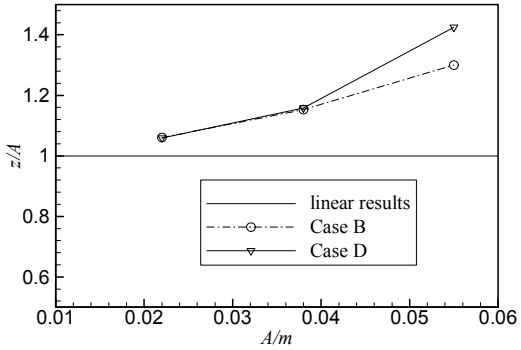

Fig. 12 Crest elevations for different amplitudes

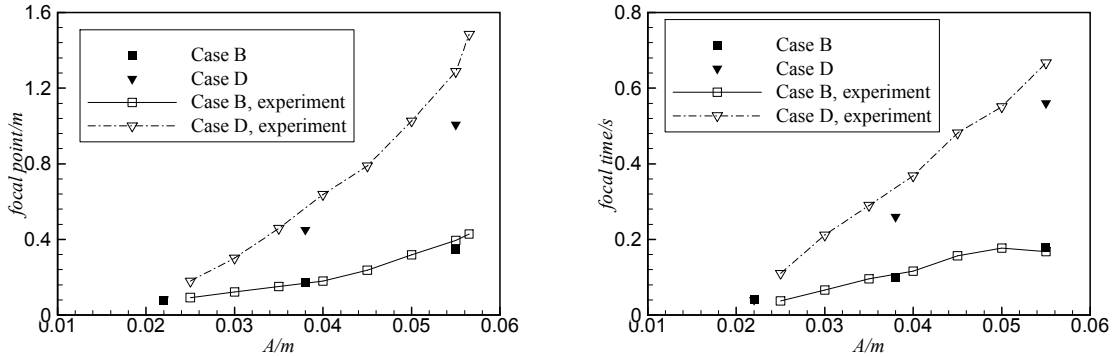

(a) (b)

Fig. 13 (a) Position of the focal points; (b) Time of focusing

3.4 Forced oscillation of a cone

During the development of the OXPOT program, a series of experiments was conducted at University College London. Their aim was to provide a high quality data base for the hydrodynamic behaviour arising when a strongly flared structure is force-oscillated according to a prescribed short transient pulse. The structure was a right circular cone oriented with its axis vertical, and it was oscillated in the vertical direction. The set-up is shown schematically in figure 14. Measurements were taken of the vertical force on the cone and the elevation (runup) of the free surface at its intersection with

the circular waterline of the cone. The programme of experiments and some of the data analysis are described in Drake et al (2009).

These experimental data allow comparisons to be made with numerical models such as OXPOT. The interaction of the free surface with a strongly flared structure provides a major challenge for such codes, because the flare can give rise to a thin jet running up the wall of the structure, and can also lead to waves rapidly overturning as they radiate away from the structure. Overturning cannot be modelled by potential flow solvers such as OXPOT, and incipient overturning is likely to give rise to rapidly developing instability in the numerical model. Neither jetting nor overturning are such an issue for wall-sided structures, particularly when the fluid motions at the waterline are predominantly vertical. But tests on a cone provide a very good test of the performance of numerical models.

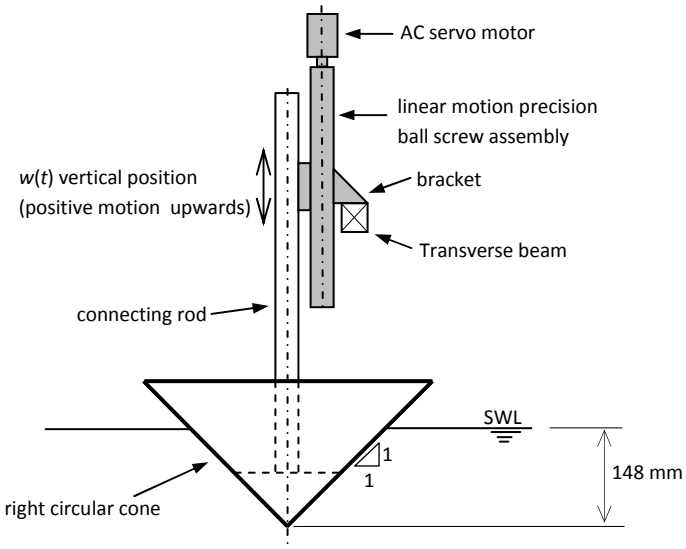

Fig. 14 Schematic showing cone and linear motion system (from Drake et al 2009)

In the experiments at UCL, the cone was driven with a transient motion following the profile of a NewWave focussed group based on a Gaussian spectrum. A range of central frequencies of the spectrum was investigated, and two values of the peak imposed motion amplitude at the crest. A typical result is shown in figure 15, and more results may be found in Drake et al (2009). Here the

time histories of the measured force and elevation (solid lines) are compared with the results of linear theory (dotted line) and the OXPOT nonlinear model (dashed line). The three sets of results diverge about one cycle after the maximum, because the far-field geometry and the resulting reflections are completely different in each case. The experiment is conducted in a rectangular wave tank; the linear model assumes the open sea; and the nonlinear model considers a circular tank (with no beach), the diameter of which is the short side of the experimental wave tank. A discussion of the difference between these three scenarios, with further results showing the effects of reflections, has been given by Eatock Taylor, Taylor and Drake (2009). In terms of interpretation of the influence of nonlinearities and comparisons of behaviour around the maximum forces and responses, the effects of reflections are not relevant, because the reflected waves have not yet had time to return back from the walls to the cone. This is a good illustration of the great effectiveness of this type of transient testing in limited sized experimental facilities (and, correspondingly, runs of numerical models over limited times).

The results shown in Figure 15 indicate that the experimental data are not symmetric about the maximum (unlike the input motion and the output linear results). One may also note the steepening of the crest and flattening of the troughs normally associated with nonlinear wave behaviour; and that the nonlinear model yields results significantly closer to the experimental data than the linear model. At the highest central frequencies of the spectrum and at the higher amplitude of forcing, however, the nonlinear model was unable to provide satisfactory results. These cases led to instabilities arising at the flared waterline, associated with much steeper waves being radiated away from the cone.

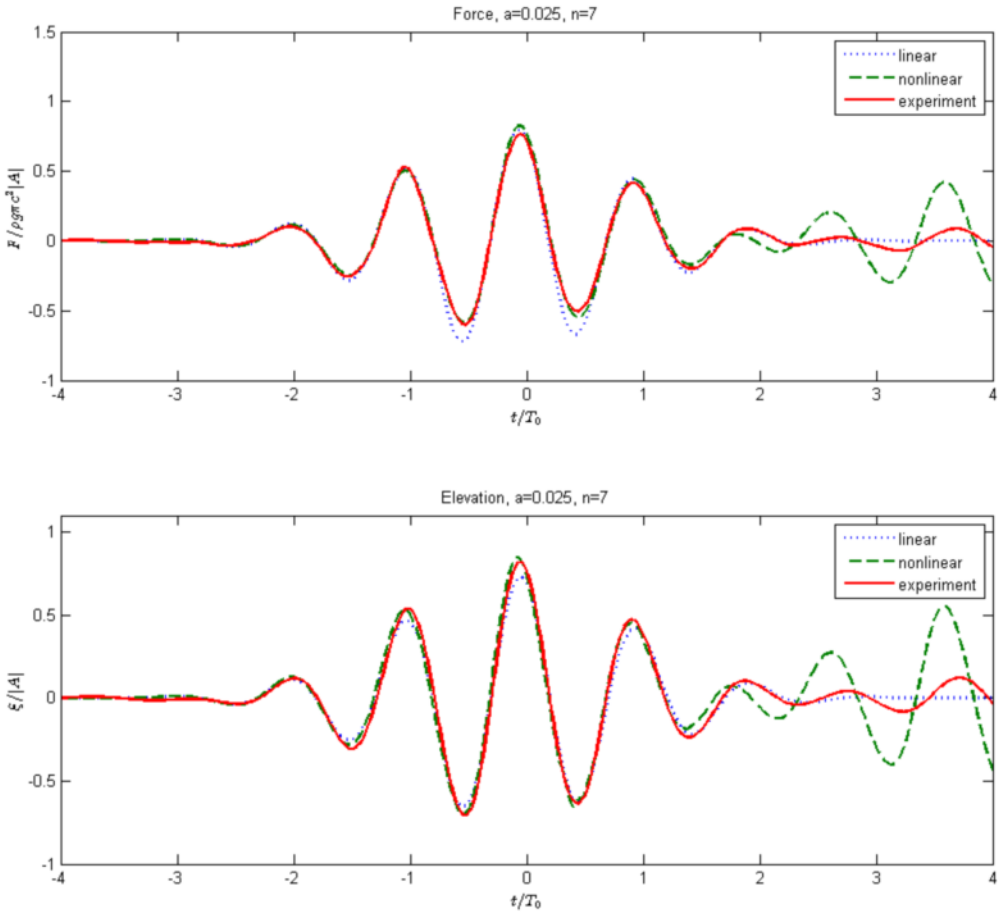

Fig. 15 Comparisons of linear and nonlinear simulations with experimental results

4. Implementation of nonlinear modelling programme in the PerAWaT project

The previous two sections have provided details concerning the nonlinear methodology and the OXPOT computer **program** which will be employed in the PerAWaT programme. Now we address the stages in the application of the nonlinear model. Each stage described below is linked to one of the WG1WP1 deliverables (D8-D14).

4.1 Non-linear analysis of free floating (uncontrolled) point absorbers (D8 "Report on non-linear hydrodynamics of free floating devices")

Results will be calculated and presented for the fully nonlinear responses of single uncontrolled axisymmetric devices in regular waves, responding in multiple degrees of freedom. The device will be modelled as a freely floating truncated cylinder, with the geometry spanning a range of radius/draught ratios. The input excitation (after an initial transient has passed the cylinder) will be regular waves, covering a range of frequencies and steepnesses. The cylinder will be on the centre line of a long wave tank, and the waves generated by a piston wavemaker. At least two different tank widths will be selected, and consideration given to different methods of generating the waves. The water depth will be selected such that the range of wave frequencies corresponds to both deep and finite water depth conditions. Practically realistic scenarios will be covered, but the results in this deliverable will be presented in non-dimensional form. This will facilitate the discussion of results (forces, motion responses and wave runup) and the understanding of behaviour (e.g. influences of geometry and nonlinearity).

Results will also be obtained for fixed truncated cylinders, and compared with calculation using linear theory (based on Yeung 1981) and second order theory (Eatock Taylor and Huang 1997, Huang and Eatock Taylor 1996) for open sea conditions. These results include first and second order forces, as well as first and second order wave runup.

Additional results will be obtained for "rounded" cylinders, defined as truncated cylinders to which a hemisphere of the same radius has been attached at the bottom. These would have draughts chosen such that the displaced volume of the rounded cylinder is the same as for the "equivalent" truncated cylinder (i.e the rounded cylinder is of deeper total draught than the equivalent truncated cylinder).

The methodology for undertaking this work will involve extensive checks of mesh quality, convergence, time stepping, beach/damping layer specification and any other parameters deemed to be relevant to the quality of the computed results.

4.2 Non-linear analysis of free floating (uncontrolled) arrays of point absorbers (D9 "Report on nonlinear analysis of an array of free floating devices")

Results will be calculated and presented for fully nonlinear responses of an array of four uncontrolled axisymmetric devices in regular waves. Similar calculations will be made to those described above for single devices (though it is anticipated that a reduced number of cases will be required, as a result of the understanding obtained in deliverable WG1WP1 D8 concerning the influence of certain parameters). The cylinders will be assumed to move freely, without any mechanical connection to earth or to its neighbours. At least three different cylinder spacings will be investigated, covering the anticipated range from weak to strong near-trapping effects (as predicted on the basis of linear theory and bottom seated cylinders). The results will be assessed with a view to establishing the degree to which nonlinear effects might be influenced by proximity of the cylinders. If the effect is small, it might be of interest to consider the outcome of constraining the response of the cylinders in one or more degrees of freedom.

Comparisons will be made with linear results obtained by GH within the scope of work for deliverable WG1WP1 D2 (the frequency domain methodology).

4.3 Array analysis of controlled devices with PTO (D10 "Report on controlled devices in regular waves")

Results will be calculated and presented for fully nonlinear responses and power take-off from controlled axisymmetric devices in regular waves. Devices in isolation and groups in square arrays of four units will be assessed , using lessons learnt in the work leading to deliverables D8 and D9 respectively. Linear and nonlinear PTOs will be considered, along with different control strategies. These will include Scenarios 1 and 2 (passive and active control) specified in table 5.1 of the D1 Methodology report by GH. PTO control systems are described in detail in WG1 WP1 D1 section 3.6.1. In the work for deliverable D10 they will be represented by mathematical expressions linked to the device motions: these expressions may be nonlinear, and involve inequalities (e.g. latching). The mooring will be represented by nonlinear springs in each relevant degree of freedom of the array (c.f. the discussion in WG1 WP1 D1 section 3.6.4), and it is anticipated that the data concerning these as well as the control systems will be available from the GH models.

4.4 Nonlinear analysis of single controlled devices in irregular seas (D11 "Report on single controlled device in irregular seas")

The control of single axisymmetric devices in irregular waves will be investigated and reported on and results presented: i.e. the effect of different control strategies on the performance of single axisymmetric devices in irregular waves; and the effect of different linear and nonlinear PTOs.

Alternative methods of generating irregular waves will be investigated. In the first method, the numerical tank described above will be used, driven by a piston or flap wavemaker. The piston will be controlled by a signal designed to generate irregular waves as in a physical tank. The requirement is to generate steep events at the location of the WEC. The piston control signal can be synthesised using superposition of spectral components (as described, for example, in section 2.7.1 of WP1 WG1 D1) combined with the wavemaker transfer function. Waves of various steepnesses will be obtained by appropriate scaling. There will, however, be no a priori control of the shape of steep events at the location of the device, because of the effects of nonlinear dispersion and the limitation of the wavemaker transfer function. There are also other limitations in using an approach such as this, because of the substantial computational resources required to perform the long runs required to achieve robust statistics.

Alternatively, instead of modelling a piston or paddle, one may specify the wave input by means of an appropriate velocity profile distributed vertically on the input boundary. This approach was used, for example, by Ning et al (2009). The method may be coupled with the idea of using a transient wave packet (e.g. as discussed in Section 3.3). Small waves are generated at the input boundary, but by appropriate focussing of these waves (due to dispersion), steep waves can be created at the location of the device. In Ning et al (2009) the kinematics at the input boundary are second order, i.e. the initial condition contains only linear and 2nd order terms. Fig. 16 from their paper shows the realised wave frequency spectrum for a particular run based on this approach, plotted on a logarithmic scale vertically. The case corresponds to moderately steep waves. The 2nd order sum and difference harmonics are clear, immediately on either side of the main spectral peak. At higher frequencies, the third and fourth order spectral peaks are clearly visible located around 2.5 and 3.3 Hz, and the fifth order sum harmonic is just apparent around 4.2 Hz. It is reassuring that a numerical simulation based on 2nd order theory contains these higher harmonics. This is because real water waves do! In this paper numerically generated time histories and spectra were compared with equivalent waves generated in an experimental flume. For the same case illustrated in Fig. 16, the

corresponding comparisons are shown in Figs. 17a and 17b. This and other comparisons lead to the conclusion that fully nonlinear wave packets as measured experimentally can be successfully reproduced by the proposed approach using a second order input at the boundary of the fluid domain.

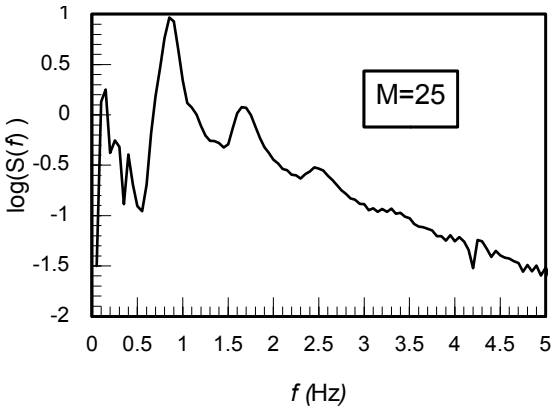

Fig. 16 Harmonic structure in wave spectrum measured at the focus point (from Ning et al 2009)

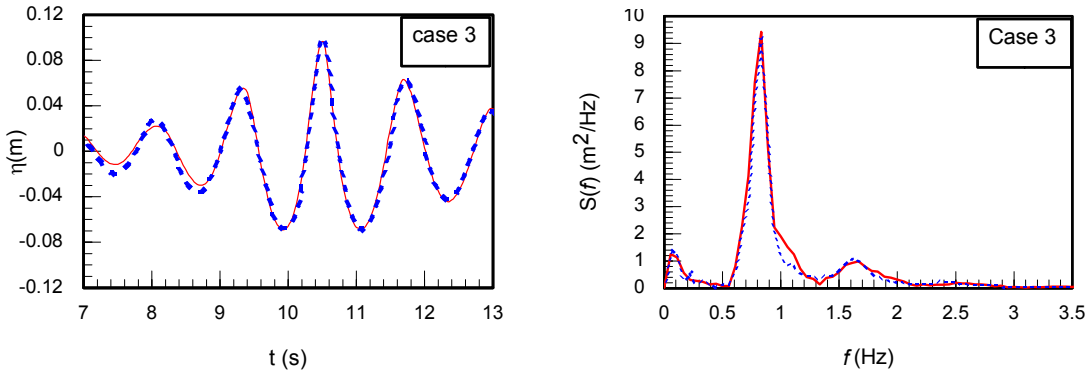

Fig. 17 Comparisons of experimental and numerical results for a moderately steep crest focussed group: a) time histories; b) spectra (from Ning et al 2009)

A third method is to embed a focussed wave group (e.g. NewWave) into a random wave train, as originally described by Taylor et al (1995). Cassidy et al (2001) implemented this approach in the context of a study of the nonlinear soil structure interaction problem of a jackup structure, and the

following is largely based on their description. The mathematical formulation of NewWave is first reviewed, followed by a summary of constraining NewWave into a random background.

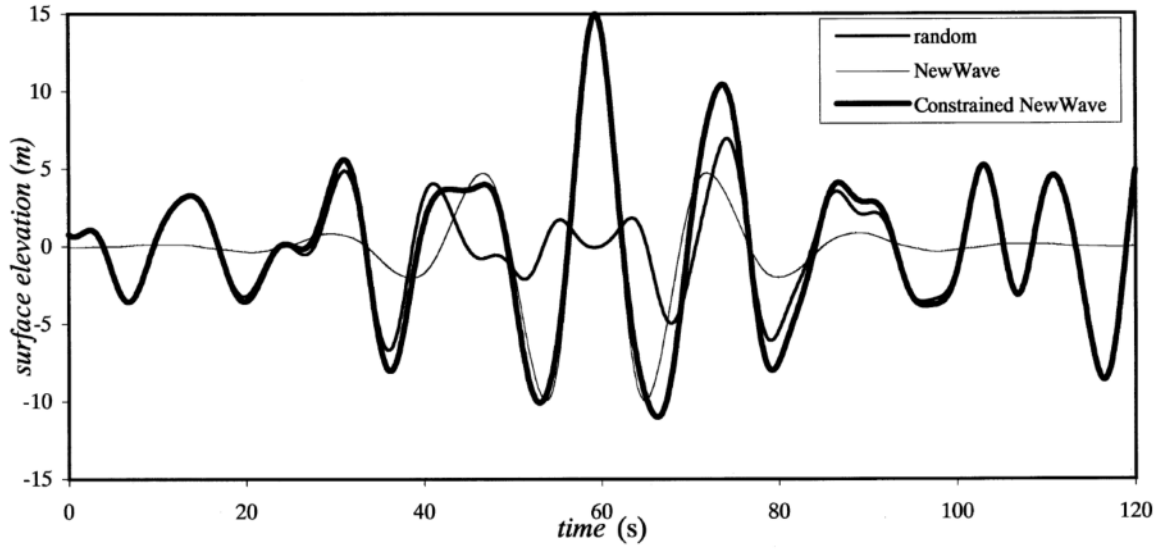

Fig. 18 Surface elevation of a NewWave group embedded in a random sea-state (from Cassidy et al 2001)

The surface elevation around an extreme crest is modelled by the statistically most probable shape associated with its occurrence. It was shown by Tromans et al. (1991) that the surface elevation is normally distributed about this most probable shape, with the surface elevation described by two terms, one deterministic and one random. As a function of time, the surface elevation can be written as

$$\eta(\tau)=\alpha r(\tau) + g(\tau) \tag{45}$$

where $\tau=t-t_1$, the time relative to the initial position of the crest (i.e. t_1 is the time when the extreme event occurs). In Eq. (45), the first term represents the most probable value, where α is the crest elevation defined as the vertical distance between the wave maximum and the mean water-level, and $r(\tau)$ is the autocorrelation function for the ocean surface elevation. The autocorrelation is proportional to the inverse Fourier Transform of the surface energy spectrum, allowing the surface elevation to be determined efficiently. The second term of Eq. (45) is a non-stationary Gaussian process with a mean of zero and a standard deviation that increases from zero at the crest to σ, the standard deviation of the underlying sea at a distance away from the crest. Therefore, as the crest

elevation increases, the first term becomes dominant and can be used alone in the derivation of surface elevation and wave kinematics near the crest.

The continuous time autocorrelation function is defined as:

$$r(\tau) = \frac{1}{\sigma^2} \int_0^\infty S_{\eta\eta}(\omega) \mathrm{e}^{\mathrm{i}\omega\tau} \, d\omega \tag{46}$$

with the time history of the extreme wave group proportional to $r(\tau)$ at the region around τ=0. For a time lag of τ =0, the autocorrelation function reduces to unity, allowing the surface elevation of the NewWave to be scaled efficiently. This is shown below in Eq. (47)

The NewWave shape can be discretised by a finite number (N) of component sinusoidal waves, leading to the discrete form:

$$\eta(X,\tau) = \frac{\alpha}{\sigma^2} \sum_{n=1}^{N} \{S_{\eta\eta}(\omega_n) d\omega \cos(k_n X - \omega_n \tau) \tag{47}$$

where k_n is the wavenumber of the nth component. X=x−x_1 is the distance relative to the initial position with X=0 representing the wave crest. This allows the positioning of the spatial field such that the crest occurs at a user-defined position relative to the structure, a useful tool in the time domain analysis.

By constraining a NewWave having a pre-determined height within a completely random background, NewWave theory can be used to produce a time series of a random surface elevation. This is performed in a mathematically rigorous manner such that the constrained sequence is statistically indistinguishable from the original random sequence. The details of a procedure achieving this are outlined by Taylor et al. (1995). Figure 18 shows the surface elevation of a NewWave with a crest elevation of 15 m embedded in a random sea-state characterised by H_s=12 m and T_z=10 s. The wave has been constrained such that its peak occurs at about 60 s. In this example, the influence of the NewWave on the surface elevation is contained within 40 s of the constrained peak.

The three approaches described above will be implemented with spectra corresponding to long-crested seas. In addition, short crested spectra will be considered, and the influence of directional spread will be investigated. Parameters to be evaluated include time histories of device responses,

and instantaneous power. Average power absorbed in the PTO during each simulation will also be computed. It is not expected that significant numbers of very long simulations will be undertaken, and it may be desirable to define an appropriate measure of average power over a limited segment of a transient wave packet. In a NewWave test one could obtain the average power defined over the length of record spanning, say, two crests on either side of the maximum; or the up and down crossings on either side of these. In simulations using a constrained NewWave one could define the average power over say 5 cycles on either side of the maximum (defining cycle on the basis of the average period for the seastate).

4.5 Nonlinear analysis of controlled array in irregular seas (D12 "Report on controlled arrays in irregular seas")

The control of arrays in irregular waves will be investigated and reported on and results presented: i.e. the effect of different control strategies on the performance of arrays in irregular waves. The methodology will be the same as that described for deliverable D11. Arrays of four units (as in D10) will be investigated, as well as a long line of units. The latter will allow much stronger near-trapping effects to be considered than arise in arrays of just 4 devices.

4.6 Comparison of nonlinear models with experimental data (D13 "Report on comparisons with experiments from WG2")

Results from the model will be compared with experiments conducted by other participants in the project (QUB and possible subcontractors in WG2), and conclusions drawn on the accuracy of fully nonlinear analysis in predicting measured behaviour. These comparisons are expected to be linked to the work on arrays of four axisymmetric bodies in regular and irregular waves. Cases of both uncontrolled and controlled arrays will be compared (D10 and D11), over a range of wave conditions from mild to more severe.

Sources of difference between theory and experiment can be expected to arise due to the effects of fluid viscosity. These would be larger for truncated cylinders than for rounded cylinders (defined in Section 4.1), due to the effects of flow separation in the former case. Furthermore, based on experiments which have been undertaken with arrays of fixed cylinders, it can be expected that the near-trapping effects in the experiment could be smaller than predicted with the ideal flow model, because of the additional damping due to skin friction and separation (Kashiwagi and Ohwatari 2002, Kagemoto et al. 2002); but the effects should still be strongly observable in appropriate cases.

4.7 Comparison between linear and non-linear analyses for both single devices and arrays (D14 “Validation report”)

An assessment will be made of the accuracy of the linear and fully nonlinear approaches to particular FDCs and events (moderate seas related to performance conditions; extreme seas related to survivability conditions) and conclusions drawn on the ranges of validity of linear wave analysis. An assessment will be provided of how much further nonlinear modelling can represent, and therefore predict, real conditions.

Comparison will be made with results reported by GH in WG1 WP1 D4 based on linearised hydrodynamics. This work will involve detailed assessment using results reported by UOx in deliverables D11 and D12. The Validation Report will seek to clarify issues relevant to the design procedure for WEC arrays that may arise from the initial comparisons between analyses based on linear and nonlinear hydrodynamics. Where appropriate additional simulations will be undertaken and reported on in order to increase confidence in the conclusions drawn.

References

Arina R, Falossi M. (2004) Domain decomposition technique for aeroacoustic simulations. Appl Numer Math 49: 263-275.

Bai W., Eatock Taylor R. (2006) Higher-order boundary element simulation of fully nonlinear wave radiation by oscillating vertical cylinders. Appl. Ocean Res. 28(4), 247-265.

Bai W., Eatock Taylor R. (2007) Numerical simulation of fully nonlinear regular and focused wave diffraction around a vertical cylinder using domain decomposition. Appl. Ocean Res. 29(1-2), 55-71.

Bai, W., Eatock Taylor, R. (2009) Fully nonlinear simulation of wave interaction with fixed and floating flared structures. Ocean Engineering 36, 223-236.

Baldock T. E, Swan C., Taylor P.H. (1996) A laboratory study of nonlinear surface waves on water. Phil. Trans. of the Royal Society of London Ser. A354, 649-676.

Boo S. Y. (2002) Linear and nonlinear irregular waves and forces in a numerical wave tank. Ocean Eng. 29, 475-493.

Borthwick A. L. G., Hunt A. C., Feng T., Taylor P. H., Stansby P.K. (2006) Flow kinematics of focused wave groups on a plane beach in the U.K. Coastal Research Facility. Coastal Engineering 53, 1033-1044

Cai X., Pedersen G.K, Langtangen H.P. (2005)A parallel multi-subdomain strategy for solving Boussinesq water wave equations. Advances in Water Resources 28, 215-233.

Cassidy, M.J., Eatock Taylor, R., Houlsby, G.T. (2001) Analysis of jack-up units using a constrained NewWave methodology. Applied Ocean Research 23, 221-234

Chern M. J., Borthwick A. G. L., Eatock Taylor R. (2001) Simulation of non-linear free surface motions in a cylindrical domain using a Chebyshev-Fourier spectral collocation method. Int J Numer Meth Fluids 36, 465-496.

Contento G. (2000) Numerical wave tank computations of nonlinear motions of two-dimensional arbitrarily shaped free floating bodies. Ocean Eng. 27, 531-556.

Cruz, J., Sykes, R., Siddorn, P., Eatock Taylor, R. (2009) Wave farm design: preliminary studies on the influences of wave climate, array layout and farm control. Proceedings of the 8th European Wave and Tidal Energy Conference, Uppsala, Sweden, pp. 736-745

De Haas P.C.A., Zandbergen P.J. (1996) The application of domain decomposition to time-domain computations of nonlinear water waves with a panel method. J. Comp. Physics 129, 332-344.

Dean E. J., Glowinski R. (1999) Domain decomposition methods for mixed finite element approximations of wave problems. Computer and Math with Appl 38, 207-214.

Drake, K. R., Eatock Taylor, R., Taylor, P. H., Bai, W. (2009) On the hydrodynamics of bobbing cones. Ocean Engineering 36, 1270-1277

Eatock Taylor, R. (2007) On modelling the diffraction of water waves. The 2005/6 Georg Weinblum Memorial Lecture, J Ship Tech Research 54, 54-80

Eatock Taylor R, Chau F. P. (1992) Wave diffraction theory – some developments in linear and non-linear theory. J Offshore Mech and Arctic Eng 114, 185-194.

Eatock Taylor, R., Huang, J. B. (1997) Second-order wave diffraction by an axisymmetric body in monochromatic waves. Proc. R. Soc. Lond. A453, 1515-1541.

Eatock Taylor R., Hung S. M. (1987) Second-order diffraction forces on a vertical cylinder in regular waves. Appl Ocean Res 9, 19-30.

Eatock Taylor, R., Meylan, M. H. (2007) Theory of scattering frequencies applied to near-trapping by cylinders. Proceedings of Twenty Second International Workshop on Water Waves and Floating Bodies, Plitvice, Croatia.

Eatock Taylor, R., Taylor, P. H. Drake, K. R. (2009) Tank wall reflections in transient testing. Proceedings of Twenty Fourth International Workshop on Water Waves and Floating Bodies, Zelenogorsk, Russia.

Eatock Taylor, R., Wu, G. X., Bai, W., Hu, Z. Z. (2008) Numerical wave tanks based on finite element and boundary element modelling. Journal of Offshore Mechanics and Arctic Engineering, 130, 031001/1-8.

Evans, D.V. and Porter, R. (1997) Near-trapping of waves by circular arrays of vertical cylinders, Applied Ocean Research 19, 83-99.

Faltinsen, O., Newman, J.N., Vinje, T. (1995), Nonlinear wave loads on a slender vertical cylinder, J. Fluid Mechanics 289, 179-198

Farhat C, Li J. (2005) An iterative domain decomposition method for the solution of a class of indefinite problems in computational structural dynamics. Appl Numer Math 54, 150-166.

Ferrant P., Le Touzé D., Pelletier K. (2003) Nonlinear time-domain models for irregular wave diffraction about offshore structures. Int. J. Numer. Meth. Fluids 43, 1257-1277.

Fochesato C, Dias F. (2006) A fast method for nonlinear three-dimensional free-surface waves. Proc R Soc Lond A462, 2715–2735.

Grilli S.T., Guyenne P., Dias F. (2001) A fully non-linear model for three-dimensional overturning waves over an arbitrary bottom. Int. J. Numer. Meth. Fluids 35, 829-867.

Grilli ST, Guyenne P, Dias F. (2001) A fully non-linear model for three-dimensional overturning waves

over an arbitrary bottom. Int J Numer Meth Fluids 35, 829-867.

Guo Y, Jin X, Ding J. (2006) Parallel numerical simulation with domain decomposition for seismic response analysis of shield tunnel. Advance in Eng Software 37, 450-456.

Guzina B.B, Pak R.Y.S, Martinez-Castro A.E. (2006) Singular boundary elements for three-dimensional elasticity problems. Engineering Analysis with Boundary Elements 30, 623-639.

Hu P.X., Wu G.X., Ma Q.W. (2002) Numerical simulation of nonlinear wave radiation by a moving vertical cylinder. Ocean Eng. 29, 1733-1750.

Huang, J.B., Eatock Taylor, R. (1996). Semi-analytical solution for the second-order wave diffraction by a truncated cylinder in monochromatic waves. J.Fluid Mech. 319, 171-196.

Isaacson M, Cheung KF. (1992) Time-domain second-order wave diffraction in three dimensions. J Waterway, Port, Coastal & Ocean Eng, ASCE 118, 496-516.

Isaacson M., Ng J.Y.T. (1993) Second-order wave radiation of three-dimensional bodies by time-domain method. Int. J. Offshore and Polar Eng. 3, 264-272.

Isaacson M., Ng J.Y.T. (1995) Time-domain second-order wave interaction with three-dimensional floating bodies. Int. J. Offshore and Polar Eng. 5, 171-179.

Kagemoto, H., Murai, M., Saito, M., Molin, B., Malenica, Š. (2002). Experimental and theoretical analysis of the wave decay along a long array of vertical cylinders. J. Fluid Mechanics 456, 113-135.

Kashiwagi, M., Ohwatari, Y. (2002) Spatial Distribution of the Wave Around Multiple Floating Bodies. Proc. 12th Int. Symp. Offshore and Polar Engineering, Kitakyushu, Japan, pp.479-486.

Kim M. H, Yue D. K. P. (1989) The complete second-order diffraction solution for an axisymmetric body. Part 1. Monochromatic incident waves. J Fluid Mech 200, 235-264.

Kim Y., Kring D. C., Sclavounos P. D. (1997) Linear and nonlinear interactions of surface waves with bodies by a three- dimensional Rankine panel method. Appl Ocean Res 19, 235-249.

Koo W., Kim M.H. (2004) Freely floating-body simulation by a 2D fully nonlinear numerical wave tank. Ocean Eng. 31, 2011-2046.

Lee C.C., Liu Y.H., Kim C.H. (1994) Simulation of nonlinear wave and forces due to transient and steady motion of submerged sphere. Int. J. Offshore and Polar Eng. 4, 174-182.

Linton, C. M. and Evans, D. V. (1990) The interaction of waves with arrays of vertical circular cylinders, J. Fluid Mechanics 215, pp.549-569.

Liu YJ, Nishimura N (2005) The fast multipole boundary element method for potential problems – a tutorial. Eng. Anal. Bound. Elem. 30, 371–381.

Longuet-Higgins M.S., Cokelet C.D. (1976) The deformation of steep surface waves on water, I. A

numerical method of computation. Proc. R. Soc. Lond. A 350, 1-26.

Ma Q.W., Wu G.X., Eatock Taylor R. (2001a) Finite element simulation of fully non-linear interaction between vertical cylinders and steep waves - part 1, methodology and numerical procedure. Int. J. Numer. Meth. Fluids 36, 265-285.

Ma Q.W., Wu G.X., Eatock Taylor R. (2001b) Finite element simulation of fully non-linear interaction between vertical cylinders and steep waves - part 2, Numerical results and validation. Int. J. Numer. Meth. Fluids 36, 287-308.

Maiti S., Sen D. (2001) Nonlinear heave radiation forces on two-dimensional single and twin hulls. Ocean Eng. 28, 1031-1052.

Malenica, Š., Eatock Taylor, R. and Huang, J. B. (1999) Second order water wave diffraction by an array of vertical cylinders, J. Fluid Mechanics 390, pp.349-373.

Malenica S, Molin B. (1995) Third-harmonic wave diffraction by a vertical cylinder. J Fluid Mech 302, 203–229.

Maniar, H. D. and Newman, J. N. (1997) Wave diffraction by a long array of cylinders, J. Fluid Mechanics 339, pp.309-330.

Meylan, M. H., Eatock Taylor, R. (2009) Time-dependent water-wave scattering by arrays of cylinders and the approximation of near trapping. Journal of Fluid Mechanics 631, 103-125.

Molin B. (1979) Second-order diffraction loads upon three-dimensional bodies. Appl Ocean Res 1, 197-202.

Newman J.N. (1990) Second-harmonic wave diffraction at large depths. J Fluid Mech 213, 59-70.

Ning, D. Z., Zang, J., Liu, S. X., Eatock Taylor, R., Teng, B., Taylor, P. H. (2009) Free surface evolution and wave kinematics for nonlinear uni-directional focused wave groups. Ocean Engineering 36, 1226-1243.

Nishimura N. (2002) Fast multipole accelerated boundary integral equation methods. Appl Mech Rev 55, 299–324.

Rokhlin V. (1985) Rapid solution of integral equations of classical potential theory. J Comp Physics 60, 187-207.

Saad Y., Schultz M. H. (1986) GMRES, A generalized minimal residual algorithm for solving non-symmetric linear systems. SIAM J Sci Stat Comput 7, 856-869.

Shen, L., Liu, Y. J. (2007) An adaptive fast multipole boundary element method for three-dimensional potential problems. Comput. Mech. 39, 681–691.

Siddorn, P., Eatock Taylor, R. (2008) Diffraction and independent radiation by an array of floating

cylinders. Ocean Engineering 35, 1289–1303

Subia SR, Ingber MS, Mitra AK. (1995) A comparison of the semidiscontinuous element and multiple node with auxiliary boundary collocation approaches for the boundary element method. Engineering Analysis with Boundary Elements 15, 19-27.

Subramanian G, Raveendra VVS, Gopolakrishna (1994) K. Robust boundary triangulation and Delaunay triangulation of arbitrary planar domains. Int J Numer Meth Eng 37, 1779-1789.

Tanizawa K. (1996) Long time fully nonlinear simulation of floating body motions with artificial damping zone. J. Soc. Naval Arch. Japan 180, 311-319.

Taylor, P. H., Jonathan, P., Harland, L. A. (1995). Time domain simulation of jack-up dynamics with the extremes of a Gaussian process. Proc. 14th Int. Conf. on Offshore Mechanic and Arctic Engineering (OMAE), Vol. 1-A, pp. 313-319.

Teng B., Kato S. (2002) Third order wave force on axisymmetric bodies. Ocean Eng 29, 815-843.

Tromans PS, Anaturk AR, Hagemeijer P. (1991) A new model for the kinematics of large ocean waves-applications as a design wave. In Proceedings of the 1st Int Offshore and Polar Eng Conf, Edinburgh, UK. 3, pp. 64-71.

Turnbull M.S., Borthwick A.G.L., Eatock Taylor R. (2003) Numerical wave tank based on a σ–transformed finite element inviscid flow solver. Int. J. Numer. Meth. Fluids 42, 641-663.

Walker, D. A. G., Eatock Taylor, R., Taylor, P. H., Zang, J. (2008) Wave diffraction and near-trapping by a multi-column gravity based structure. Ocean Engineering 35, 201-229

Walker, D. A. G., and Eatock Taylor, R. (2005) Wave diffraction from linear arrays of cylinders, Ocean Engineering 32, 2053-2078

Wang C.Z., Wu G.X. (2007) Time domain analysis of second-order wave diffraction by an array of vertical cylinders Journal of Fluids and Structures 23, 605–631

Wang, C. Z. and Wu, G. X. (2010) Interactions between fully nonlinear water waves and cylinder arrays in a wave tank. Ocean Engineering 37, 400-417.

Wang P., Yao Y., Tulin M.P. (1995) An efficient numerical tank for non-linear water waves, based on the multi-subdomain approach with BEM. Int. J. Numer. Meth. Fluids 20, 1315-1336.

Wu G.X., Eatock Taylor R. (1994) Finite element analysis of two dimensional non-linear transient water waves. Appl. Ocean Res. 16, 363-372.

Wu GX, Eatock Taylor R. (2003) The coupled finite element and boundary element analysis of nonlinear interactions between waves and bodies. Ocean Eng 30, 387-400.

Wu GX, Eatock Taylor R. (1989) The numerical solution of the motions of a ship advancing in waves.

In, Proceedings of the 5th Proc Int Conf on Numerical Ship Hydrodynamics, Hiroshima, Japan pp. 386-394.

Wu GX, Eatock Taylor R. (1995) Time stepping solutions of the two-dimensional nonlinear wave radiation problem. Ocean Eng 22, 785-798.

Wu G.X., Eatock Taylor R. (1996) Transient motion of a floating body in steep water waves. Proceedings of Eleventh International Workshop on Water Waves and Floating Bodies, Hamburg.

Wu GX, Hu ZZ. (2004) Simulation of nonlinear interactions between waves and floating bodies through a finite-element-based numerical tank. Proc R Soc Lond A 460, 2797-2817.

Xue M, Xü H, Liu Y, Yue DKP. (2001) Computations of fully nonlinear three-dimensional wave-wave and wave-body interactions. Part 1. Dynamics of steep three-dimensional waves. J Fluid Mech 438, 11–39.

Yeung R. W. (1981) Added mass and damping of a vertical cylinder in finite-depth waters. Appl Ocean Res 3, 119-133.

Zhao Y, Graham JMR. (1996) An iterative method for boundary element solution of large offshore structures using the GMRES solver. Ocean Eng 23(6), 483-495.